Galaxy evolution in the metric of the Cosmic Web

K. Kraljic, S. Arnouts, C. Pichon, C. Laigle, S. de La Torre, D. Vibert, C. Cadiou, Y. Dubois, M. Treyer, C. Schimd, et al.

Monthly Notices
of the
ROYAL ASTRONOMICAL SOCIETY

MNRAS **474,** 547–571 (2018)
Advance Access publication 2017 October 10

doi:10.1093/mnras/stx2638

Galaxy evolution in the metric of the cosmic web

K. Kraljic,[1]★ S. Arnouts,[1] C. Pichon,[2,3] C. Laigle,[4] S. de la Torre,[1] D. Vibert,[1] C. Cadiou,[2] Y. Dubois,[2] M. Treyer,[1] C. Schimd,[1] S. Codis,[5] V. de Lapparent,[2] J. Devriendt,[4] H. S. Hwang,[6] D. Le Borgne,[2] N. Malavasi,[7] B. Milliard,[1] M. Musso,[2,8] D. Pogosyan,[9] M. Alpaslan,[10] J. Bland-Hawthorn[11] and A. H. Wright[12]

[1]*Aix Marseille University, CNRS, LAM, Laboratoire d'Astrophysique de Marseille, Marseille, France*
[2]*Institut d'Astrophysique de Paris, UMR 7095 CNRS et Université Pierre et Marie Curie, 98bis Bd Arago, F-75014, Paris, France*
[3]*School of Physics, Korea Institute for Advanced Study (KIAS), 85 Hoegiro, Dongdaemun-gu, Seoul, 02455, Republic of Korea*
[4]*Sub-department of Astrophysics, University of Oxford, Keble Road, Oxford OX1 3RH, United Kingdom*
[5]*Canadian Institute for Theoretical Astrophysics, University of Toronto, 60 St. George Street, Toronto, ON M5S 3H8, Canada*
[6]*Quantum Universe Center, Korea Institute for Advanced Study (KIAS), 85 Hoegiro, Dongdaemun-gu, Seoul 02455, Republic of Korea*
[7]*Department of Physics and Astronomy, Purdue University, 525 Northwestern Avenue, West Lafayette, IN 47907, USA*
[8]*Institut de physique théorique, Université Paris Saclay and CEA, CNRS, 91191 Gif-sur-Yvette, France*
[9]*Department of Physics, University of Alberta, 412 Avadh Bhatia Physics Laboratory, Edmonton, AB T6G 2J1, Canada*
[10]*NASA Ames Research Center, Moffett Field, Mountain View, CA 94035, USA*
[11]*Sydney Institute for Astronomy, School of Physics, University of Sydney, NSW 2006, Australia*
[12]*Argelander-Institut für Astronomie (AIfA), Universität Bonn, Auf dem Hügel 71, D-53121 Bonn, Germany*

Accepted 2017 October 6. Received 2017 September 8; in original form 2017 July 19

ABSTRACT

The role of the cosmic web in shaping galaxy properties is investigated in the Galaxy And Mass Assembly (GAMA) spectroscopic survey in the redshift range $0.03 \leq z \leq 0.25$. The stellar mass, $u - r$ dust corrected colour and specific star formation rate (sSFR) of galaxies are analysed as a function of their distances to the 3D cosmic web features, such as nodes, filaments and walls, as reconstructed by DisPerSE. Significant mass and type/colour gradients are found for the whole population, with more massive and/or passive galaxies being located closer to the filament and wall than their less massive and/or star-forming counterparts. Mass segregation persists among the star-forming population alone. The red fraction of galaxies increases when closing in on nodes, and on filaments regardless of the distance to nodes. Similarly, the star-forming population reddens (or lowers its sSFR) at fixed mass when closing in on filament, implying that some quenching takes place. These trends are also found in the state-of-the-art hydrodynamical simulation HORIZON-AGN. These results suggest that on top of stellar mass and large-scale density, the traceless component of the tides from the anisotropic large-scale environment also shapes galactic properties. An extension of excursion theory accounting for filamentary tides provides a qualitative explanation in terms of anisotropic assembly bias: at a given mass, the accretion rate varies with the orientation and distance to filaments. It also explains the absence of type/colour gradients in the data on smaller, non-linear scales.

Key words: large-scale structure of Universe – cosmology: observations – galaxies: evolution – galaxies: high-redshift – galaxies: statistics.

1 INTRODUCTION

Within the Λ cold dark matter (ΛCDM) cosmological paradigm, structures in the present-day Universe arise from hierarchical clustering, with smaller dark matter haloes forming first and progressively merging into larger ones. Galaxies form by the cooling and condensation of baryons that settle in the centres of these haloes (White & Rees 1978) and their spin is predicted to be correlated with that of the halo generated from the tidal field torques at the moment of proto-halo collapse (tidal torque theory, TTT; e.g. Peebles 1969; Doroshkevich 1970; Efstathiou & Jones 1979; White 1984). However, dark matter haloes, and galaxies residing within them, are not isolated. They are part of a larger-scale pattern, dubbed the cosmic web (Jõeveer, Einasto & Tago 1978; Bond, Kofman & Pogosyan 1996), arising from the anisotropic collapse

★E-mail: katarina.kraljic@lam.fr

of the initial fluctuations of the matter density field under the effect of gravity across cosmic time (Zel'dovich 1970).

This web-like pattern, brought to light by systematic galaxy redshift surveys (e.g. De Lapparent, Geller & Huchra 1986; Geller & Huchra 1989; Colless et al. 2001; Tegmark et al. 2004), consists of large nearly-empty void regions surrounded by sheet-like walls framed by filaments which intersect at the location of clusters of galaxies. These are interpreted as the nodes, or high-density peaks of the large-scale structure pattern, containing a large fraction of the dark matter mass (Bond et al. 1996; Pogosyan et al. 1996). The baryonic gas follows the gravitational potential gradients imposed by the dark matter distribution, then shocks and winds up around multistream, vorticity-rich filaments (Codis et al. 2012; Hahn, Angulo & Abel 2015; Laigle et al. 2015). Filamentary flows, along specific directions dictated by the geometry of the cosmic web, advect angular momentum into the newly formed low mass galaxies with spins typically aligned with their neighbouring filaments (Pichon et al. 2011; Stewart et al. 2013). The next generation of galaxies forms through mergers as they drift along these filaments towards the nodes of the cosmic web with a post merger spin preferentially perpendicular to the filaments, having converted the orbital momentum into spin (e.g. Aubert, Pichon & Colombi 2004; Navarro, Abadi & Steinmetz 2004; Aragón-Calvo et al. 2007b; Codis et al. 2012; Libeskind et al. 2012; Trowland, Lewis & Bland-Hawthorn 2013; Aragon-Calvo & Yang 2014; Dubois et al. 2014; Welker et al. 2015).

Within the standard paradigm of hierarchical structure formation based on ΛCDM cosmology (Blumenthal et al. 1984; Davis et al. 1985), the imprint of the (*past*) large-scale environment on galaxy properties is therefore, to some degree, expected via galaxy mass assembly history. Intrinsic properties, such as the mass of a galaxy (and internal processes that are directly linked to its mass), are indeed shaped by its build-up process, which in turn is correlated with its *present* environment. For instance, more massive galaxies are found to reside preferentially in denser environments (e.g. Dressler 1980; Postman & Geller 1984; Kauffmann et al. 2004; Baldry et al. 2006). This mass-density relation can be explained through the biased mass function in the vicinity of the large-scale structure (LSS; Kaiser 1984; Efstathiou et al. 1988) where the enhanced density of the dark matter field allows the proto-halo to pass the critical threshold of collapse earlier (Bond et al. 1991) resulting in an overabundance of massive haloes in dense environments. However, what is still rightfully debated is whether the large-scale environment is also driving other observed trends such as morphology-density (e.g. Dressler 1980; Postman & Geller 1984; Dressler et al. 1997; Goto et al. 2003), colour-density (e.g. Blanton et al. 2003; Baldry et al. 2006; Bamford et al. 2009) or star formation-density (e.g. Hashimoto et al. 1998; Lewis et al. 2002; Kauffmann et al. 2004) relations, and galactic 'spin' properties, such as their angular momentum vector, their orientation or chirality (trailing versus leading arms).

On the one hand, there are evidences that the cosmic web affects galaxy properties. Void galaxies are found to be less massive, bluer, and more compact than galaxies outside of voids (e.g. Rojas et al. 2004; Beygu et al. 2016); galaxies infalling into clusters along filaments show signs of some physical mechanisms operating even before becoming part of these systems, that galaxies in the isotropic infalling regions do not (Porter et al. 2008; Martínez, Muriel & Coenda 2016); Kleiner et al. (2017) find systematically higher HI fractions for massive galaxies ($M_\star > 10^{11}\,\mathrm{M}_\odot$) near filaments compared to the field population, interpreted as evidence for a more efficient cold gas accretion from the intergalactic medium; Kuutma, Tamm & Tempel (2017) report an environmental transformation with a higher elliptical-to-spiral ratio when moving closer to filaments, interpreted as an increase in the merging rate or the cut-off of gas supplies near and inside filaments (see also Aragon-Calvo, Neyrinck & Silk 2016); Chen et al. (2017) detect a strong correlation of galaxy properties, such as colour, stellar mass, age and size, with the distance to filaments and clusters, highlighting their role beyond the environmental density effect, with red or high-mass galaxies and early-forming or large galaxies at fixed stellar mass having shorter distances to filaments and clusters than blue or low-mass and late-forming or small galaxies, and Tojeiro et al. (2017) interpret a steadily increasing stellar-to-halo mass ratio from voids to nodes for low mass haloes, with the reversal of the trend at the high-mass end, found for central galaxies in the GAMA survey (Driver et al. 2009, 2011), as an evidence for halo assembly bias being a function of geometric environment. At higher redshift, a small but significant trend in the distribution of galaxy properties within filaments was reported in the spectroscopic survey VIPERS ($z \simeq 0.7$; Malavasi et al. 2017) and with photometric redshifts ($0.5 < z < 0.9$) in the COSMOS field (with a 2D analysis; Laigle et al. 2017). Both studies find significant mass and type segregations, where the most massive or quiescent galaxies are closer to filaments than less massive or active galaxies, emphasizing that large-scale cosmic flows play a role in shaping galaxy properties.

On the other hand, Alpaslan et al. (2015) find in the GAMA data that the most important parameter driving galaxy properties is stellar mass as opposed to environment (see also Robotham et al. 2013). Similarly, while focusing on spiral galaxies alone, Alpaslan et al. (2016) do find variations in the star formation rate (SFR) distribution with large-scale environments, but they are identified as a secondary effect. Another quantity tracing different geometric environments that was found to vary is the luminosity function. However, while Guo, Tempel & Libeskind (2015) conclude that the filamentary environment may have a strong effect on the efficiency of galaxy formation (see also Benítez-Llambay et al. 2013), Eardley et al. (2015) argue that there is no evidence of a direct influence of the cosmic web as these variations can be entirely driven by the underlying *local* density dependence. These discrepancies are partially expected: the present state of galaxies must be impacted by the effect of the past environment, which in turn does correlate with the present environment, if mildly so, but these environmental effects must first be distinguished from mass-driven effects which typically dominate.

The TTT, naturally connecting the large-scale distribution of matter and the angular momentum of galactic haloes (e.g. Jones & Efstathiou 1979; Barnes & Efstathiou 1987; Heavens & Peacock 1988; Porciani, Dekel & Hoffman 2002a,b; Lee 2004), in its recently revisited, conditioned formulation (Codis, Pichon & Pogosyan 2015) predicts the angular momentum distribution of the forming galaxies relative to the cosmic web, which tend to first have their angular momentum aligned with the filament's direction while the spin orientation of massive galaxies is preferentially in the perpendicular direction. Despite the difficulty to model properly the halo-galaxy connection, due to the complexity, non-linearity and multiscale character of the involved processes, modern cosmological hydrodynamic simulations confirm such a mass-dependent angular momentum distribution of galaxies with respect to the cosmic web (Dubois et al. 2014; Welker et al. 2014, 2017). On galactic scales, the dynamical influence of the cosmic web is therefore traced by the distribution of angular momentum and orientation of galaxies, when measured relative to their embedding large-scale environment. The impact of such environment on the spins of galaxies has

only recently started to be observed (confirming the spin alignment for spirals and preferred perpendicular orientation for ellipticals; Trujillo et al. 2006; Lee & Erdogdu 2007; Paz et al. 2008; Tempel et al. 2013; Tempel & Libeskind 2013; Pahwa et al. 2016, but see also Jones, van de Weygaert & Aragón-Calvo 2010; Cervantes-Sodi, Hernandez & Park 2010; Andrae & Jahnke 2011, for contradictory results). What is less obvious is whether observed integrated scalar properties such as morphology or physical properties (SFR, type, metallicity, which depend not only on the mass but also on the past and present gas accretion) are also impacted.

Theoretical considerations alone suggest that local density as a sole and unique parameter (and consequently any isotropic definition of the environment based on density alone) is not sufficient to account for the effect of gravity on galactic scale (e.g. Mo, van den Bosch & White 2010) and therefore capture the environmental diversity in which galaxies form and evolve: one must also consider the relative past and present orientation of the tidal tensor with respect to directions pointing towards the larger-scale structure principal axes. At the simplest level, on large scales, gravity should be the dominant force. Its net cumulative impact is encoded in the tides operating on the host dark matter halo. Such tides may be decomposed into the trace of the tidal tensor, which equals the local density, and its traceless part, which applies distortion and rotation to the forming galaxy. The effect of the former on increasing scales has long been taken into account in standard galaxy formation scenarios (Kaiser 1984), while the effect of the latter has only recently received full attention (e.g. Codis et al. 2015). Beyond the above-discussed effect on angular momentum, other galaxy's properties could in principle be influenced by the large-scale traceless part of the tidal field, which modifies the accretion history of a halo depending on its location within the cosmic web. For instance, the tidal shear near saddles along the filaments feeding massive haloes is predicted to slow down the mass assembly of smaller haloes in their vicinity (Hahn et al. 2009; Borzyszkowski et al. 2017; Castorina et al. 2016). Bond & Myers (1996) integrated the effect of ellipsoidal collapse (via the shear amplitude), which may partially delay galaxy formation, in the Extended Press-Schechter (EPS) theory. Yet, in that formulation, the geometry of the delay imposed by the specific relative orientation of tides imposed by the large-scale structure is not accounted for, because time delays are ensemble-averaged over all possible geometries of the LSS. The anisotropy of the large-scale cosmic web – voids, walls, filaments, and nodes (which shape and orient the tidal tensor beyond its trace) – should therefore be taken into account explicitly, as it impacts mass assembly. Despite of the above-mentioned difficulty in properly describing the connection between galaxies and their host dark matter haloes, this anisotropy should have direct observational signatures in the differential properties of galaxies with respect to the cosmic web at fixed mass and local density. Quantifying these signatures is the topic of this paper. Extending EPS to account for the geometry of the tides beyond that encoded in the density of the field is the topic of the companion paper (Musso et al. 2017).

This paper explores the impact of the cosmic web on galaxy properties in the GAMA survey, using the Discrete Persistent Structure Extractor code (DisPerSE; Sousbie 2011; Sousbie, Pichon & Kawahara 2011) to characterize its 3D topological features, such as nodes, filaments and walls. GAMA is to date the best data set for this kind of study, given its unique spectroscopic combination of depth, area, target density and high completeness, as well as its broad multiwavelength coverage. Variations in stellar mass and colour, red fraction and star formation activity are investigated as a function of galaxy distances to these three features. The rest of the paper is organized as follows. Section 2 summarizes the data and describes the sample selection. The method used to reconstruct the cosmic web is presented in Section 3. Section 4 investigates the stellar-mass and type/colour segregation and the star formation activity of galaxies within the cosmic web. Section 5 shows how these results compare to those obtained in the HORIZON-AGN simulation (Dubois et al. 2014). Section 6 addresses the impact of the density on the measured gradients towards filaments and walls. Results are discussed in Section 7 jointly with predictions from Musso et al. (2017). Finally, Section 8 concludes. Additional details on the matching technique and the impact of the boundaries to the measured gradients are provided in Appendices A and B, respectively. Appendix C investigates the effect of smoothing scale on the found gradients, Appendix D briefly presents the HORIZON-AGN simulation, Appendix F provides tables of median gradients and a short summary of predicted gradient misalignments is presented in Appendix E.

Throughout the study, a flat ΛCDM cosmology with $H_0 = 67.5\,\mathrm{km\,s^{-1}\,Mpc^{-1}}$, $\Omega_M = 0.31$ and $\Omega_\Lambda = 0.69$ is adopted (Planck Collaboration XIII 2016). All statistical errors are computed by bootstrapping, such that the errors on a given statistical quantity correspond to the standard deviation of the distribution of that quantity re-computed in 100 random samples drawn from the parent sample with replacement. All magnitudes are quoted in the AB system, and by log we refer to the 10-based logarithm.

2 DATA AND DATA PRODUCTS

This section describes the observational data and derived products, namely the galaxy and group catalogues, that have been used in this work.

2.1 Galaxy catalogue

The analysis is based on the GAMA survey[1] (Driver et al. 2009, 2011; Hopkins et al. 2013; Liske et al. 2015), a joint European-Australian project combining multiwavelength photometry (UV to far-IR) from ground and space-based facilities and spectroscopy obtained at the Anglo-Australian Telescope (AAT, NSW, Australia) using the AAOmega spectrograph. GAMA provides spectra for galaxies across five regions, but this work only considers the three equatorial fields G9, G12 and G15 covering a total area of 180 $\mathrm{deg^2}$ ($12 \times 5\,\mathrm{deg^2}$ each), for which the spectroscopic completeness is >98 per cent down to a *r*-band apparent magnitude $m_r = 19.8$. The reader is referred to Wright et al. (2016) for a complete description of the spectro-photometric catalogue constructed using the LAMBDAR[2] code that was applied to the 21-band photometric data set from the GAMA Panchromatic Data Release (Driver et al. 2016), containing imaging spanning the far-UV to the far-IR.

The physical parameters for the galaxy sample such as the absolute magnitudes, extinction corrected rest-frame colours, stellar masses and specific star formation rate (sSFR) are derived using a grid of model spectral energy distributions (SED; Bruzual & Charlot 2003) and the SED fitting code LEPHARE[3] (Arnouts et al. 1999; Ilbert et al. 2006). The details used to derive these physical parameters are given in the companion paper (Treyer et al. in preparation).

[1] http://www.gama-survey.org/
[2] Lambda Adaptive Multi-Band Deblending Algorithm in *R*.
[3] http://cesam.lam.fr/lephare/lephare.html

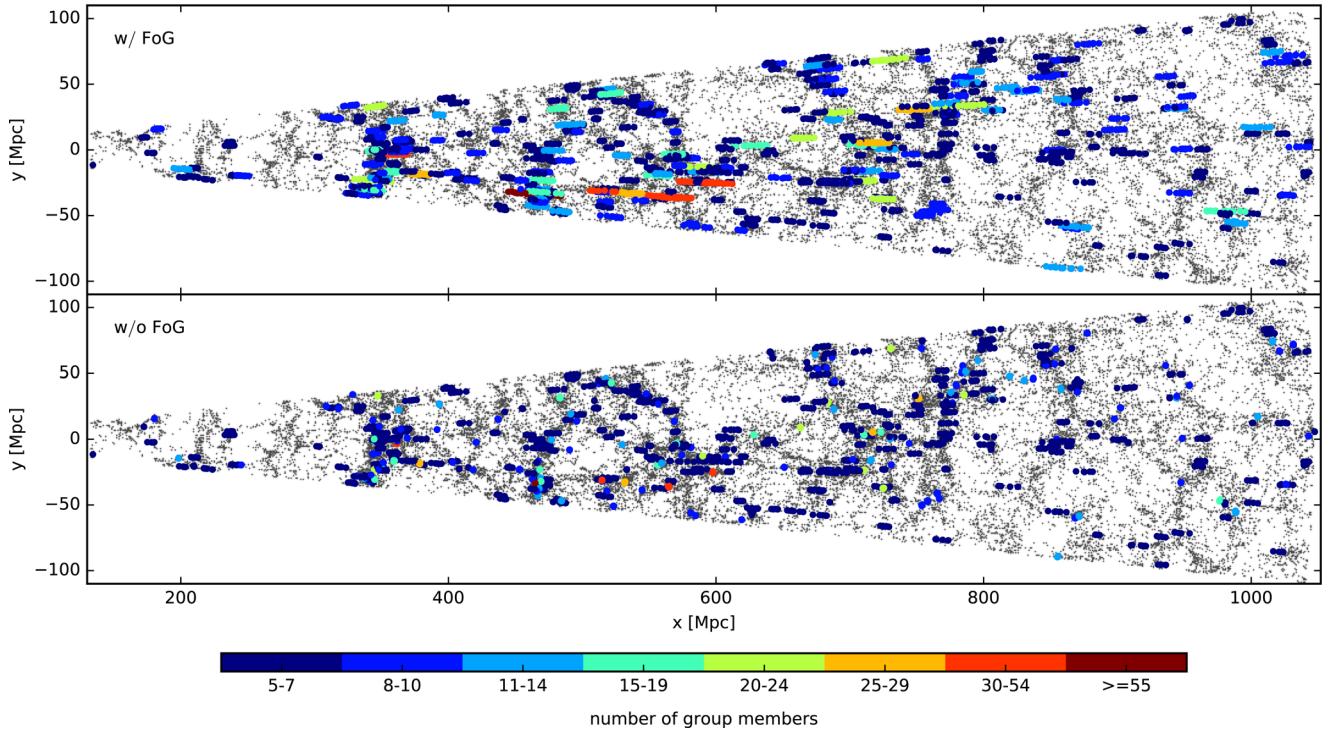

Figure 1. Spatial distribution of whole galaxy population with $m_r < 19.8$ in the GAMA field G12 in the redshift range $0.03 \leq z \leq 0.25$ (grey points). Overplotted are galaxy group members, colour coded by the size of their group. Only groups having five or more members are shown. The top and bottom panels illustrate the galaxy group members before and after correcting for the FoG effect, respectively.

The classification between the active (star-forming) and passive (quiescent) populations is based on a simple colour cut at $u - r = 1.8$ in the rest-frame extinction corrected $u - r$ versus r diagram that is used to separate the two populations. This colour cut is consistent with a cut in sSFR at $10^{-10.8}$ yr^{-1} (see Treyer et al. in preparation). Hence, in what follows, the terms red (blue) and quiescent (star-forming) will be used interchangeably.

The analysis is restricted to the redshift range $0.03 \leq z \leq 0.25$, totalling 97 072 galaxies. This is motivated by the high galaxy sampling required to reliably reconstruct the cosmic web. Beyond $z \sim 0.25$, the galaxy number density drops substantially (to 2×10^{-3} Mpc^{-3} from 8×10^{-3} Mpc^{-3} at $z \leq 0.25$, on average), while below $z \sim 0.03$, the small volume does not allow us to explore the large scales of the cosmic web.

The stellar mass completeness limits are defined for the passive and active galaxies as the mass above which 90 per cent of galaxies of a given type (blue/red) reside at a given redshift $z \pm 0.004$. This translates into mass completeness limits of $\log(M_\star/\mathrm{M}_\odot) = 9.92$ and $\log(M_\star/\mathrm{M}_\odot) = 10.46$ for the blue and red populations at $z \leq 0.25$, respectively.

2.2 Group catalogue

Since the three-dimensional distribution of galaxies relies on the redshift-based measures of distances, it is affected by their peculiar velocities. In order to optimize the cosmic web reconstruction, one needs to take into account these redshift-space distortions. On large scales, these arise from the coherent motion of galaxies accompanying the growth of structure, causing its flattening along the line of sight, the so-called Kaiser effect (Kaiser 1987). On small scales, the so-called Fingers of God (FoG; Jackson 1972; Tully & Fisher 1978) effect, induced by the random motions of galaxies within virialized haloes (groups and clusters) causes the apparent elongation of structures in redshift space, clearly visible in the galaxy distribution in the GAMA survey (Fig. 1, top panel). While the Kaiser effect tends to enhance the cosmic web by increasing the contrast of filaments and walls (e.g. Subba Rao et al. 2008; Shi et al. 2016), the FoG effect may lead to the identification of spurious filaments. Because the impact of the Kaiser effect is expected to be much less significant than that of the FoG (e.g. Subba Rao et al. 2008; Kuutma et al. 2017), for the purposes of this work, we do not attempt to correct for it and we focus on the compression of the FoG only. To do so, the galaxy groups are first constructed with the use of an anisotropic Friends-of-Friends (FoF) algorithm operating on the projected perpendicular and parallel separations of galaxies, that was calibrated and tested using the publicly available GAMA mock catalogues of Robotham et al. (2011) (see also Merson et al. 2013, for details of the mock catalogues construction). Details on the construction of the group catalogue and related analysis of group properties can be found in the companion paper (Treyer et al. in preparation). Next, the centre of each group is identified following Robotham et al. (2011) (see also Eke et al. 2004, for a different implementation). The method is based on an iterative approach: first, the centre of mass of the group (CoM) is computed; next its projected distance from the CoM is found iteratively for each galaxy in the group by rejecting the most distant galaxy. This process stops when only two galaxies remain and the most massive galaxy is then identified as the centre of the group. The advantage of this method, as shown in Robotham et al. (2011), is that the iteratively defined centre is less affected by interlopers than luminosity-weighted centre or the central identified as the most luminous group galaxy. The groups are then compressed radially so that the dispersions in transverse and radial directions are equal, making the galaxies in the groups isotropically distributed about their centres (see e.g. Tegmark et al. 2004). In practice, since

the elongated FoG effect affects mostly the largest groups, only groups with more than six members are compressed. Note that the precise correction of the FoG effect is not sought. What is needed for the purpose of this work is the elimination of these elongated structures that could be misidentified as filaments.

Fig. 1 displays the whole galaxy population and the identified FoF groups (coloured by their richness) in the GAMA field G12. The top and bottom panels show the groups before and after correcting for the FoG effect, respectively. For the sake of clarity, only groups having at least five members are shown. The visual inspection reveals that most of the groups are located within dense regions, often at the intersection of the apparently filamentary structures.

3 THE COSMIC WEB EXTRACTION

With the objective of exploring the impact of the LSS on the evolution of galaxy properties, one first needs to properly describe the main components of the cosmic web, namely the high-density peaks (nodes) which are connected by filaments, framing the sheet-like walls, themselves surrounding the void regions. Among the various methods developed over the years, two broad classes can be identified. One uses the geometrical information contained in the *local* gradient and the Hessian of the density or potential field (e.g. Novikov, Colombi & Doré 2006; Aragón-Calvo et al. 2007a,b; Hahn et al. 2007a,b; Sousbie et al. 2008a,b; Forero-Romero et al. 2009; Bond, Strauss & Cen 2010a,b), while the second exploits the topology and connectivity of the density field by using the watershed transform (Aragón-Calvo, van de Weygaert & Jones 2010) or Morse theory (e.g. Colombi, Pogosyan & Souradeep 2000; Sousbie et al. 2008a; Sousbie 2011). The theory for the former can be built in some details, (see e.g. Pogosyan et al. 2009), shedding some light on physical interpretation, while the latter avoids shortcomings of a second-order Taylor expansion of the field and provides a natural metric in which to compute distances to filaments. Within these broad categories, some algorithms deal with discrete data sets, while others require that the density field must be first estimated (possibly on multiple scales). An exhaustive description of several cosmic web extraction techniques and a comparison of their classification patterns as measured in simulations are presented in Libeskind et al. (2017). While this paper found some differences between the various algorithms, which should in principle be accounted for as modelling errors in this work, these differences remain small on the scales considered.

3.1 Cosmic web with disperse

This work uses the Discrete Persistent Structure Extractor (DisPerSE; see Sousbie et al. 2011, for illustrations in a cosmological context), a geometric three-dimensional ridge extractor dealing directly with discrete data sets, making it particularly well adapted for astrophysical applications. It allows for a scale and parameter-free coherent identification of the 3D structures of the cosmic web as dictated by the large-scale topology. For a detailed description of the DisPerSE algorithm and its underlying theory, the reader is referred to Sousbie (2011); its main features are summarized below.

DisPerSE is based on discrete Morse and persistence theories. The Delaunay tessellation is used to generate a simplicial complex, i.e. a triangulated space with a geometric assembly of cells, faces, edges and vertices mapping the whole volume. The Delaunay Tessellation Field Estimator (DTFE; Schaap & van de Weygaert 2000; Cautun & van de Weygaert 2011) allows for estimating the density field at each vertex of the Delaunay complex. The Morse theory enables to extract from the density field the critical points, i.e. points with a vanishing (discrete) gradient of the density field (e.g. maxima, minima and saddle points). These critical points are connected via the field lines tangent to the gradient field in every point. They induce a geometrical segmentation of space, where all the field lines have the same origin and destination, known as the Morse complex. This segmentation defines distinct regions called ascending and descending k-manifolds.[4] The morphological components of the cosmic web are then identified from these manifolds: ascending 0-manifolds trace the voids, ascending 1-manifolds trace the walls and filaments correspond to the ascending 2-manifolds with their extremities plugged on to the maxima (peaks of the density field). In addition to its ability to work with sparsely sampled data sets while assuming nothing about the geometry or homogeneity of the survey, DisPerSE allows for the selection of retained structures on the basis of the significance of the topological connection between critical points. DisPerSE relies on persistent homology theory to pair critical points according to the birth and death of a topological feature in the excursion. The 'persistence' of a feature or its significance is assessed by the density contrast of the critical pair chosen to pass a certain signal-to-noise threshold. The noise level is defined relative to the RMS of persistence values obtained from random sets of points. This thresholding eliminates less significant critical pairs, allowing to simplify the Morse complex, retaining its most topologically robust features. Fig. 2 shows that filaments outskirt walls, themselves circumventing voids. The filaments are made of a set of connected segments and their end points are connected to the maxima, the peaks of the density field where most of clusters and large groups reside. Each wall is composed of the facets of tetrahedra from the Delaunay tessellation belonging to the same ascending 2-manifold. In this work, DisPerSE is run on the flux-limited GAMA data with a 3σ persistence threshold. Fig. 3 illustrates the filaments for the G12 field, overplotted on the density contrast of the underlying galaxy distribution, $1 + \delta$, where the local density is estimated using the DTFE density estimator. Even in this 2D projected visualization, one can see that filaments trace the ridges of the 3D density field connecting the density peaks between them.

3.2 Cosmic web metric

Having identified the major cosmic web features, let us now define a new metric to characterize the environment of a galaxy, which will be referred to as the 'cosmic web metric' and into which galaxies are projected. Fig. 4 gives a schematic view of this framework. Each galaxy is assigned the distance to its closest filament, $D_{\rm skel}$. The impact point in the filament is then used to define the distances along the filament towards the node, $D_{\rm node}$ and towards the saddle point, $D_{\rm saddle}$. Similarly, $D_{\rm wall}$ denotes the distance of the galaxy to its closest wall. In this work, only distances $D_{\rm node}$, $D_{\rm skel}$ and $D_{\rm wall}$ are used. Other investigations of the environment in the vicinity of the saddle points are postponed to a forthcoming work.

The accuracy of the reconstruction of the cosmic web features is sensitive to the sampling of the data set. The lower the

[4] The index k refers to the critical point the field lines emanate from (ascending) or converge to (descending), and is defined as its number of negative eigenvalues of the Hessian: a minimum of the field has index 0, a maximum has index 3 and the two types of saddles have indices 1 and 2.

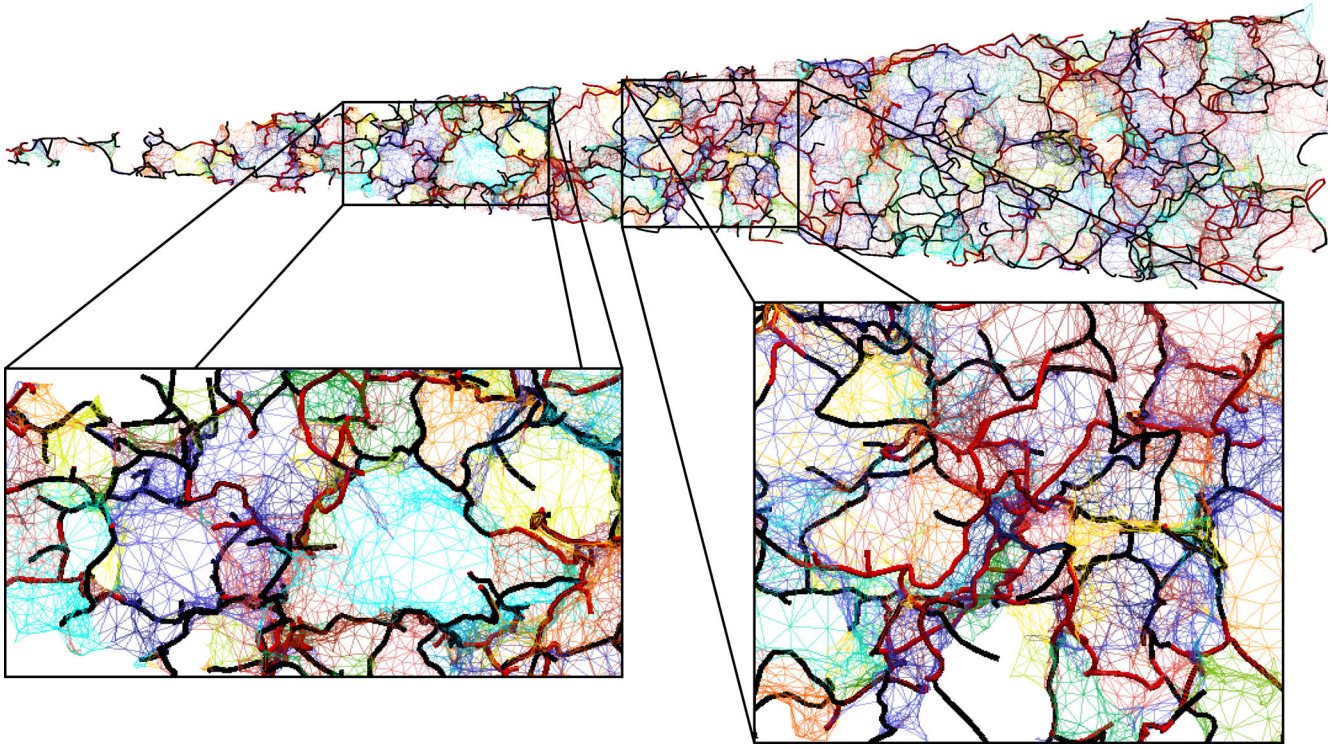

Figure 2. Illustration of the walls and filaments in the G12 field. For the sake of clarity and for the illustrative purposes, only the cosmic web features detected above a persistence threshold of 5σ are shown. Filaments are coloured in black, with the most persistent ones ($>6\sigma$) plotted in red, while walls are colour coded randomly. Note how DisPerSE is capable of recovering the important features of the underlying cosmic field by identifying its (topologically) most-robust features. In particular, it extracts filaments as a set of connected segments, which outskirt walls, themselves circumventing voids.

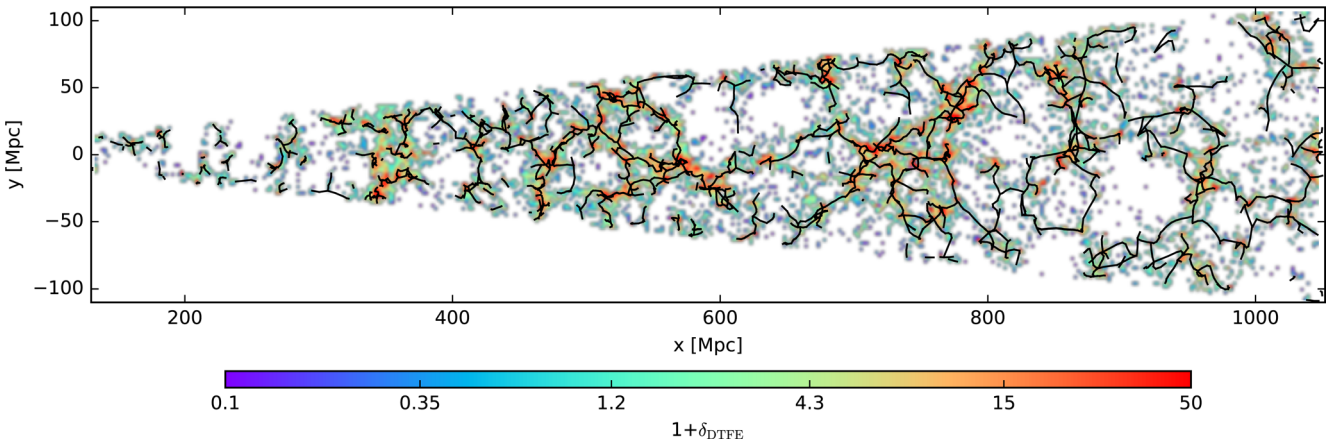

Figure 3. Illustration of the filamentary network (black lines) extracted with the DisPerSE code within the $\pm 1.2^\circ$ of the central declination of the G12 field. The persistence threshold with which the filamentary network and the associated structures, used in this work and shown here, are extracted is 3σ. Also shown is the density contrast of the underlying galaxy distribution, measured with the small-scale adaptive DTFE estimator (see the text) and averaged over cells of $2.3 \times 2.3\,\mathrm{Mpc}^2$ (white colour is used for empty cells). In spite of the projection effects, the visual inspection reveals that filaments follow the ridges of the density field which connect the peaks together.

sampling the larger the uncertainty on the location of the individual components of the cosmic web. To account for the variation of the sampling throughout the survey, unless stated differently, all the distances are normalized by the redshift-dependent mean inter-galaxy separation $\langle D_z \rangle$, defined as $\langle D_z \rangle \equiv n(z)^{-1/3}$, where $n(z)$ represents the number density of galaxies at a given redshift z. For the combined three fields of GAMA survey, $\langle D_z \rangle$ varies from 3.5 to 7.7 Mpc across the redshift range $0.03 \leq z \leq 0.25$, with a mean value of $\sim$5.6 Mpc.

4 GALAXY PROPERTIES WITHIN THE COSMIC WEB

In this section, the dependence of various galaxy properties, such as stellar mass, $u - r$ colour, sSFR and type, with respect to their location within the cosmic web is analysed. First, the impact of the nodes, representing the largest density peaks, is investigated. Next, by excluding these regions, galaxy properties are studied within the intermediate density regions near the filaments. Finally, the analysis is extended to the walls.

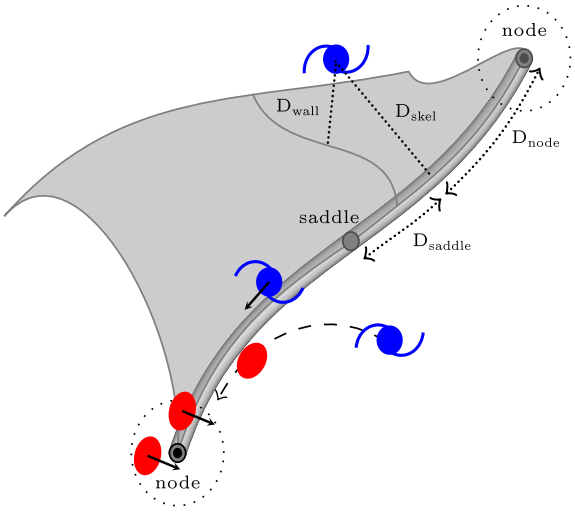

Figure 4. Schematic view of the 'cosmic web' metric in which the analysis is performed. The position of a galaxy within the cosmic web is parametrized by its distance to the closest filament, $D_{\rm skel}$, and its distance to the closest wall, $D_{\rm wall}$. $D_{\rm node}$ and $D_{\rm saddle}$ represent the distances from the impact point to the node and saddle along the corresponding filament, respectively.

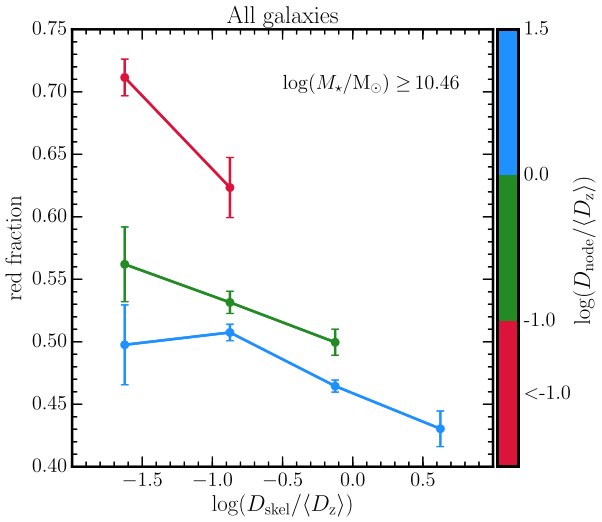

Figure 5. Red fraction of galaxies (the number of quiescent galaxies over the entire population) as a function of $D_{\rm skel}$ for three different bins of $D_{\rm node}$ as indicated by the colour. Both distances are normalized by the redshift-dependent mean inter-galaxy separation $\langle D_z \rangle$. Only galaxies with $\log(M_\star/{\rm M}_\odot) \geq 10.46$ are considered. Star-forming and quiescent populations are matched in mass (see Section 4.2.1). The error bars are calculated from 100 bootstrap samples. The fraction of red galaxies is found to increase with decreasing distances both to the closest filament $D_{\rm skel}$ and to the node of this $D_{\rm node}$. Recalling that $\langle D_z \rangle \sim 5.6$ Mpc, the fraction of passive galaxies increases at given $D_{\rm skel}$ by ∼20 per cent from several tens of Mpc away from the nodes (blue line) to less than ∼0.5 Mpc (red line). At fixed $D_{\rm node}$, the increase of the red fraction with decreasing distance to filaments is milder, of ∼10 per cent, regardless of the distance to the node.

4.1 The role of nodes via the red fractions

Let us start by analysing the combined impact of nodes and filaments on galaxies through the study of the red fractions. The red fraction, defined as the number of passive galaxies with respect to the entire population, is analysed as a function of the distance to the nearest filament, $D_{\rm skel}$ and the distance to its associated node, $D_{\rm node}$.

This analysis is restricted to galaxies more massive than $\log(M_\star/{\rm M}_\odot) \geq 10.46$, as imposed by the mass limit completeness of the passive population (see Section 2). The stellar mass distributions of the passive and star-forming populations are not identical, with the passive galaxies dominating the high mass end. Therefore, to prevent biases in the measured gradients introduced by such differences, the mass-matched samples are used. The detailed description of the mass-matching technique can be found in Appendix A1.

In Fig. 5 the red fraction of galaxies is shown as a function of $D_{\rm skel}$ in three different bins of $D_{\rm node}$. While the fraction of passive galaxies is found to increase with decreasing distances to both the filaments and nodes, the dominant effect is the distance to the nodes. At fixed $D_{\rm skel}$, the fraction of passive galaxies sharply increases with decreasing distance to the nodes. Recalling that the mean inter-galaxy separation $\langle D_z \rangle \sim 5.6$ Mpc, a 20–30 per cent increase in the fraction of passive galaxies is observed from several Mpc away from the nodes to less than ∼500 kpc. This behaviour is expected since the nodes represent the loci where most of the groups and clusters reside and reflect the well-known colour-density (e.g. Blanton et al. 2003; Baldry et al. 2006; Bamford et al. 2009) and star formation-density (e.g. Lewis et al. 2002; Kauffmann et al. 2004) relations. However, the gradual increase suggests that some physical processes already operate before the galaxies reach the virial radius of massive haloes. At fixed $D_{\rm node}$, the fraction of passive galaxies increases with decreasing distance to filaments, but this increase is milder compared to that with respect to nodes: an increase of ∼10 per cent is observed regardless of the distance to the nodes. These regions with intermediate densities appear to be a place where the transformation of galaxies takes place as emphasized in the next section.

4.2 The role of filaments

In order to infer the role played by filaments alone in the transformation of galactic properties, the impact of nodes, the high-density regions has to be mitigated. By construction, nodes are at the intersection of filaments: they drive the well-known galaxy type-density as well as stellar mass-density relations. To account for this bias, Gay et al. (2010) and Malavasi et al. (2017) adopted a method where a given physical property or distance of each galaxy was down-weighted by its local density. Laigle et al. (2017) adopted a more stringent approach by rejecting all galaxies that are too close to the nodes. This method allows us to minimize the impact of nodes, avoiding the difficult-to-quantify uncertainty of the residual contribution of the density weighting scheme. We therefore adopt the latter approach. As shown in Appendix B1, this is achieved by rejecting all galaxies below a distance of 3.5 Mpc from a node.

4.2.1 Stellar mass gradients

Fig. 6 shows the normalized probability distribution functions (PDFs) of the distance to the nearest filament $D_{\rm skel}$ in three stellar mass bins for the entire population and star-forming galaxies alone (top left-hand and right-hand panels, respectively). The medians of the PDFs, shown by vertical lines, are listed together with the corresponding error bars in Table 1. The significance of the observed trends is assessed by computing the residuals between the distributions in units of σ (bottom panels), defined as $\Delta_{1-2}/\sqrt{\sigma_1^2 + \sigma_2^2}$, where Δ_{1-2} is the difference between the PDFs of the populations 1 and 2, and σ_1 and σ_2 are the corresponding standard deviations.

For the entire population (left-hand panels), differences between the PDFs of the three stellar mass bins are observed: the most

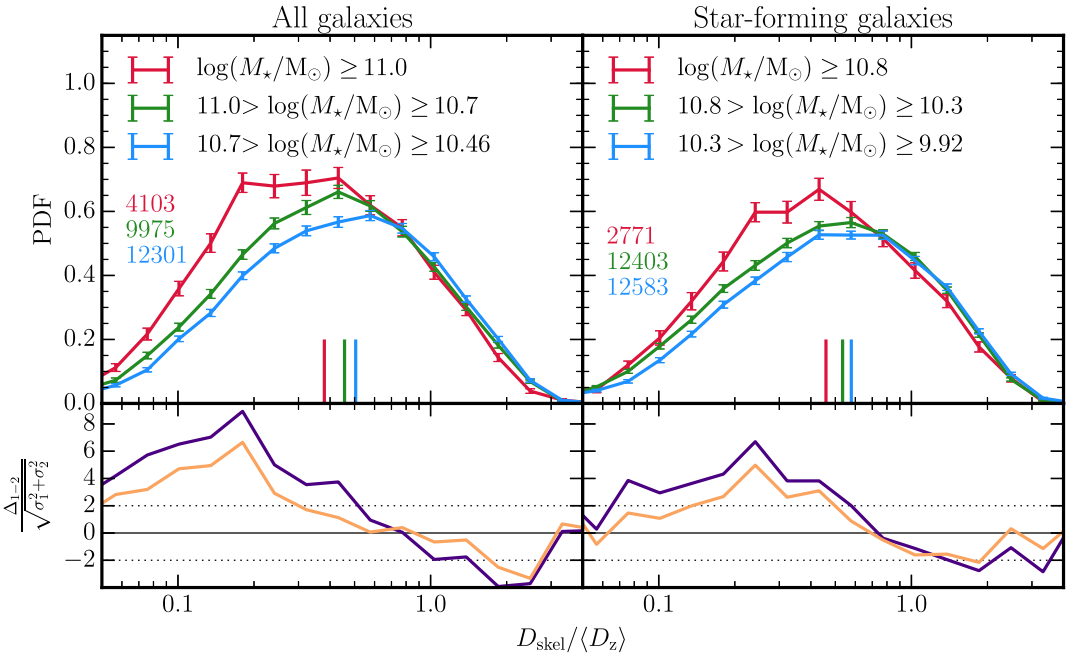

Figure 6. *Top row:* Differential distributions of the distances to the nearest filament, $D_{\rm skel}$ (normalized by $\langle D_z \rangle$, the redshift-dependent mean inter-galaxy separation) for the entire galaxy population (left-hand panel) and star-forming galaxies alone (right-hand panel) in three different stellar mass bins. Note that these bins are different for the two populations: this is due to the stellar mass completeness limit that is different (see Section 2). To highlight an effect specific to the filaments, the contribution of node is minimized (see the text for details). The vertical lines indicate the medians of the distributions and their values together with associated error bars are listed in Table 1. The numbers of galaxies in different considered bins are indicated in each panel. The error bars are calculated from 100 bootstrap samples. There is a mass segregation of galaxies with respect to filaments of the entire as well as star-forming population: more massive galaxies tend to be preferentially located closer to the filaments compared to their lower-mass counterparts. *Bottom row:* Residuals in units of σ between the two most extreme mass bins (purple line; $10.7 > \log(M_\star/{\rm M}_\odot) \geq 10.46$ and $\log(M_\star/{\rm M}_\odot) \geq 11.0$ on the left-hand panel and $10.3 > \log(M_\star/{\rm M}_\odot) \geq 9.92$ and $\log(M_\star/{\rm M}_\odot) \geq 10.8$ on the right-hand panel), and between the high and intermediate mass bins (orange solid line; $\log(M_\star/{\rm M}_\odot) \geq 11.0$ and $11.0 > \log(M_\star/{\rm M}_\odot) \geq 10.7$ on the left-hand panel and $\log(M_\star/{\rm M}_\odot) \geq 10.8$ and $10.8 > \log(M_\star/{\rm M}_\odot) \geq 10.3$ on the right-hand panel).

Table 1. Medians for the PDFs displayed in Figs 6–10.

	Selection[a]	Bin	Median[b] $D_{\rm skel}/\langle D_z \rangle$	Median[b] $D_{\rm wall}/\langle D_z \rangle$
Mass[c]	All galaxies	$\log(M_\star/{\rm M}_\odot) \geq 11$	0.379 ± 0.009	0.334 ± 0.005
		$11 > \log(M_\star/{\rm M}_\odot) \geq 10.7$	0.456 ± 0.007	0.381 ± 0.004
		$10.7 > \log(M_\star/{\rm M}_\odot) \geq 10.46$	0.505 ± 0.006	0.403 ± 0.004
	SF galaxies	$\log(M_\star/{\rm M}_\odot) \geq 11$	0.459 ± 0.012	0.385 ± 0.011
		$11 > \log(M_\star/{\rm M}_\odot) \geq 10.4$	0.534 ± 0.007	0.429 ± 0.006
		$10.4 > \log(M_\star/{\rm M}_\odot) \geq 9.92$	0.578 ± 0.007	0.453 ± 0.007
Type[d]	SF versus passive[e]	Star-forming	0.504 ± 0.008	0.411 ± 0.006
		Passive	0.462 ± 0.007	0.376 ± 0.006

Notes. [a]Panels of Figs 6–10.
[b]Medians of distributions as indicated in Figs 6–10 by vertical lines; errors represent half width at half-maximum of the bootstrap distribution, i.e. the distribution of medians from each of 100 bootstrap samples, fitted by a Gaussian curve.
[c]Figs 6 and 9.
[d]Figs 7 and 10.
[e]Only galaxies with stellar masses $\log(M_\star/{\rm M}_\odot) \geq 10.46$ are considered.

massive galaxies ($\log(M_\star/{\rm M}_\odot) \geq 11$) are located closer to the filaments than the intermediate population ($11 > \log(M_\star/{\rm M}_\odot) \geq 10.7$), while the population with the lowest stellar masses ($10.7 > \log(M_\star/{\rm M}_\odot) \geq 10.46$) is found furthest away from the filaments. The significances of the difference between the most massive and the two lowest stellar mass bins are shown in the bottom panel. Between the most extreme stellar mass bins (purple line), the difference exceeds 4σ close to the filament and 2σ at larger distances. It is slightly less significant between the intermediate and lowest stella mass bins (orange line), but still in excess of 2σ close to the filament. The differences between the PDFs can be also quantified in terms of their medians, where the differences between the highest and lowest stellar mass bins are significant at an $\sim 10\sigma$ level (see Table 1). These results confirm previous claims of a mass segregation with respect to filaments, where the most massive galaxies are located near the core of the filaments, while

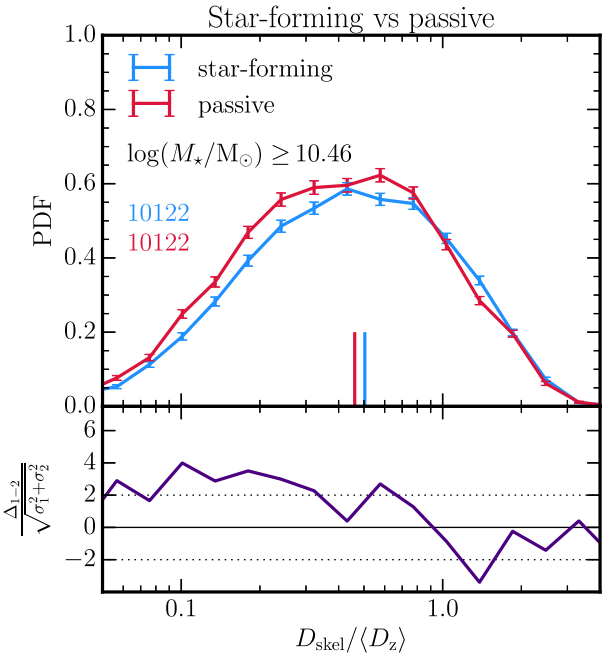

Figure 7. *Top:* Differential distributions of the distances to the nearest filament, D_{skel} (normalized by $\langle D_z \rangle$, the redshift-dependent mean inter-galaxy separation) for star-forming and quiescent galaxies that have been matched in mass (see the text for details). To highlight an effect specific to the filaments, the contribution of node is minimized (see the text for details). The vertical lines indicate the medians of the distributions and their values, together with associated error bars, are listed in Table 1. The numbers of galaxies in different considered bins are indicated in each panel. The error bars are calculated from 100 bootstrap samples. Galaxies are found to segregate, relative to filaments, according to their type: quiescent galaxies tend to be preferentially located closer to the filaments compared to their star-forming counterparts. *Bottom:* Residuals in units of σ between the star-forming and passive galaxies.

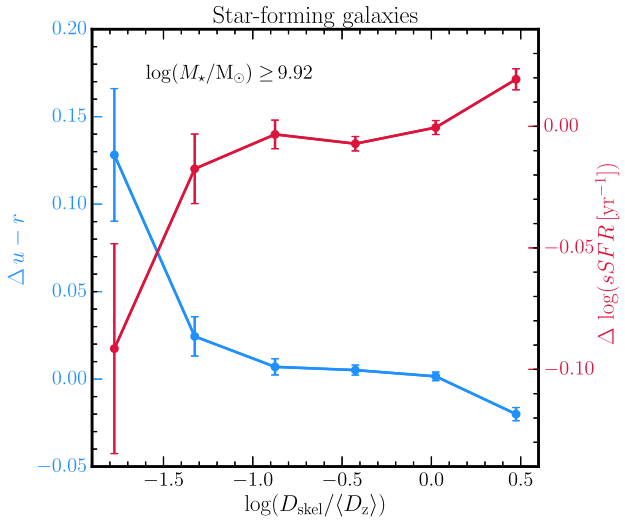

Figure 8. $u-r$ colour (blue line) and sSFR (red line) of star-forming galaxies as a function of D_{skel}. The y-axes indicate the amount by which $u-r$ colour and sSFR differ from the median values at given mass (see the text for details). Only galaxies with $\log(M_\star/\mathrm{M}_\odot) \geq 9.92$ and far-away from nodes (at $D_{\mathrm{node}} > 3.5$ Mpc) are considered. Star-forming galaxies tend to have higher $u-r$ colour (tend to be redder) and lower sSFR when they get closer to the filaments than their more distant counterparts.

the less massive ones tend to reside preferentially on their outskirts (Laigle et al. 2017; Malavasi et al. 2017). As the impact of the nodes has been minimized, it is therefore established that this stellar mass gradient is driven by the filaments themselves and not by the densest regions of the cosmic web.

The mass segregation is also found among the star-forming population alone (right-hand panels), such that more massive star-forming galaxies tend to be closer to the geometric core of the filament than their less massive counterparts. Note that the mass bins for star-forming galaxies differ from mass bins used for the entire population. The completeness stellar mass limit allows us to decrease the lowest mass bin to $\log(M_\star/\mathrm{M}_\odot) = 9.92$ when considering the star-forming galaxies alone (see Section 2). The significance of these stellar mass gradients between the extreme stellar mass bins exceeds 4σ near the filaments, while the difference of the medians reaches an $\sim 8\sigma$ level (see Table 1).

4.2.2 Type gradients

Let us now investigate the impact of the filamentary network on the type/colour of galaxies. To do so, galaxies are split by type between star-forming and passive galaxies based on the dust corrected $u-r$ colour as discussed in Section 2.1. As for the analysis of the red fraction (Section 4.1), the sample is restricted to galaxies with $\log(M_\star/\mathrm{M}_\odot) \geq 10.46$ and the star-forming and passive populations are matched in stellar mass. Fig. 7 shows the PDFs of the normalized distances D_{skel} within the mass-matched samples of star-forming and passive populations, which by construction have the same number of galaxies. Galaxies are found to segregate according to their type such that passive galaxies tend to reside in regions located closer to the core of filaments than their star-forming counterparts. The significance of the type gradients between the two populations exceeds 3σ near filaments while the difference between the medians reaches an $\sim 4\sigma$ level (see Table 1).

4.2.3 Star formation activity gradients

To explore whether the impact of filaments on the star formation activity of galaxies can be detected beyond the red fractions and type segregation reported above, the focus is now on the star-forming population alone through the study of their (dust corrected) $u-r$ colour and sSFR.

Both these quantities are known to evolve with stellar mass which itself varies within the cosmic web (see above). To remove this mass dependence, the offsets of $u-r$ colour and sSFR, $\Delta u-r$ and ΔsSFR, respectively, from the median values of all star-forming galaxies at a given mass are computed for each galaxy. Fig. 8 shows the medians of $\Delta u-r$ and ΔsSFR as a function of D_{skel}. Both quantities are found to carry the imprint of the large-scale environment. At large distances from the filaments ($D_{\mathrm{skel}} \geq 5$ Mpc), star-forming galaxies are found to be more active than the average. At intermediate distances ($0.5 \leq D_{\mathrm{skel}} \leq 5$ Mpc), star formation activity of star-forming galaxies does not seem to evolve with the distance to the filaments, while in the close vicinity of the filaments ($D_{\mathrm{skel}} \leq 0.5$ Mpc), they show signs of a decrease in star formation efficiency (redder colour and lower sSFR). The significance of these results will be discussed in Section 7.

4.3 The role of walls in mass and type gradients

Let us now investigate the impact of walls on galaxy properties. Figs 9 and 10 show the PDFs of the distances to the closest wall D_{wall} for the same selections as in Figs 6 and 7, respectively. The distances

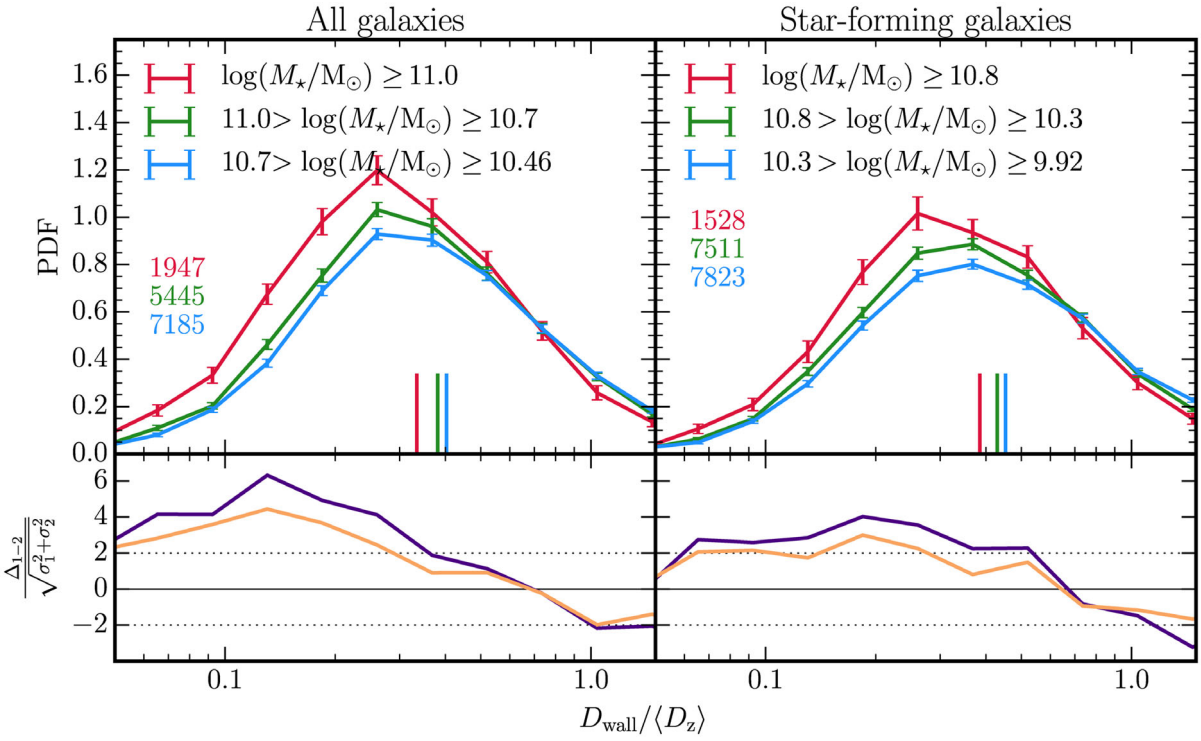

Figure 9. *Top row:* As in Fig. 6, but for the distances to the nearest wall, $D_{\rm wall}$. To minimize the contribution of nodes and filaments to the measured signal, galaxies located closer to a node than 3.5 Mpc and closer to a filament than 2.5 Mpc are removed form the analysis. There is a mass segregation of galaxies with respect to walls of the entire as well as star-forming population: more massive galaxies tend to be preferentially located closer to the filaments compared to their lower-mass counterparts. *Bottom row:* Residuals in units of σ as in Fig. 6.

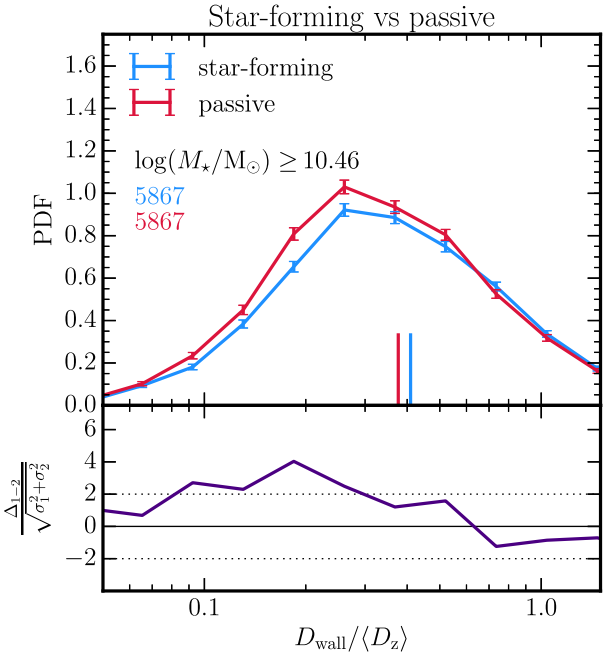

Figure 10. *Top row:* As in Fig. 7, but for the distances to the nearest wall, $D_{\rm wall}$. To minimize the contribution of nodes and filaments to the measured signal, galaxies located closer to a node than 3.5 Mpc and closer to a filament than 2.5 Mpc are removed from the analysis. Galaxies are found to segregate, with respect to walls, according to their type: quiescent galaxies tend to be preferentially located closer to the walls compared to their star-forming counterparts. *Bottom row:* Residuals in units of σ as in Fig. 7.

are again normalized by the redshift-dependent mean inter-galaxy separation $\langle D_z \rangle$. The values of medians with corresponding error bars are listed in Table 1. As for filaments, one seeks signatures induced by a particular environment solely, walls in this case. Given that filaments are located at the intersections between walls, in addition to the contamination by nodes, which is of concern for filaments, one has to make sure that the contribution of filaments themselves is minimized as well. Following the method adopted in Section 4.2.1, Appendix B2 shows that this can be achieved by removing from the analysis galaxies having distances to the nodes smaller than 3.5 Mpc and distances to the closest filaments less than 2.5 Mpc.

The derived trends are qualitatively similar to those measured with respect to filaments. Massive galaxies are located closer to walls compared to their low-mass counterparts; star-forming galaxies preferentially reside in the outer regions of walls; and mass segregation is present also among star-forming population of galaxies with more massive star-forming galaxies having smaller distances to the walls than low-mass counterparts. Since these walls typically embed smaller-scale filaments, the net effect of transverse gradients perpendicular to these filaments should add up to transverse gradients perpendicular to walls.

The significance of the measured trends, in terms of the residuals between medians (see Table 1), is above 3σ for all considered gradients, slightly lower than for the gradients towards filaments. The deviations of $\sim 10\sigma$ and $\sim 5\sigma$ are detected between the highest and lowest stellar mass bins among the whole and star-forming population alone, respectively, while between the star-forming and passive galaxies it reaches $\sim 4\sigma$, as in the case of gradients towards filaments.

Table 2. Medians for the PDFs displayed in Fig. 11.

Selection[a]	Bin	Median[b]	
		$D_{\rm skel}$ (Mpc)	$D_{\rm wall}$ (Mpc)
Mass	$\log(M_\star/{\rm M}_\odot) \geq 10.8$	1.34 ± 0.09	0.79 ± 0.04
	$10.8 > \log(M_\star/{\rm M}_\odot) \geq 10.4$	1.73 ± 0.08	1.14 ± 0.03
	$10.4 > \log(M_\star/{\rm M}_\odot) \geq 10$	1.97 ± 0.04	1.22 ± 0.02
sSFR[c]	$-10.8 > \log(sSFR/{\rm yr}^{-1})$	1.46 ± 0.07	1.02 ± 0.03
	$-10.4 > \log(sSFR/{\rm yr}^{-1}) \geq -10.8$	1.88 ± 0.06	1.18 ± 0.03
	$\log(sSFR/{\rm yr}^{-1}) \geq -10.4$	2.0 ± 0.04	1.18 ± 0.02

Notes. [a]Panels of Fig. 11.
[b]Medians of distributions as indicated in Fig. 11 by vertical lines; errors are computed as in Table 1.
[c]Only galaxies with stellar masses $\log(M_\star/{\rm M}_\odot) \geq 10$ are considered.

5 COMPARISON WITH THE HORIZON-AGN SIMULATION

In this section, a qualitative support for the results on the mass and star-formation activity segregation is provided via the analysis of the large-scale cosmological hydrodynamical simulation HORIZON-AGN (Dubois et al. 2014). Note that the main purpose of such an analysis is to provide a reference measurement of gradients in the context of a large-scale 'full physics' experiment. The construction of the GAMA-like mock catalogue is not performed because the geometry of HORIZON-AGN does not allow us to recover the entire GAMA volume and the flux-limited sample requires a precise modelling of fluxes in different bands.

A brief summary of some of the main features of the simulation can be found in Appendix D. Here, the results on the mass and sSFR gradients towards filaments and walls are presented. The HORIZON-AGN simulation is analysed at low redshift ($z \sim 0.1$), comparable to the mean redshift studied in this paper, and the same analysis is performed as in the GAMA data. The filamentary network and associated structures are extracted by running the DisPerSE code with the persistence threshold of 3σ.

Fig. 11 shows the mass (left-hand panels) and sSFR (right-hand panels) gradients towards filaments (figure a) and walls (figure b) as measured in the HORIZON-AGN simulation. The impact of the nodes and filaments on the measured signal is minimized by removing from the analysis galaxies that are closer to the node than 3.5 Mpc and closer to the filament than 1 Mpc. The detailed description of the method used to identify these cuts in distances can be found in Appendix B1. Consistently with the measurements in GAMA, galaxies in HORIZON-AGN are found to segregate by stellar mass, with more massive galaxies being preferentially closer to both the filaments and walls than their low-mass counterparts. Similarly, the presence of the sSFR gradient, whereby less star-forming galaxies tend to be closer to the cores of filaments and walls than their more star-forming counterparts, is in qualitative agreement with the type/colour gradients detected in the GAMA survey. Note that the three bins of sSFR are used to separate out the highly star-forming galaxies, with $\log({\rm sSFR/yr}^{-1}) \geq -10.4$, from passive ones, with $\log({\rm sSFR/yr}^{-1}) < -10.8$, in order to compare with the type gradients in the observations. In the simulation, sSFR is a more reliable parameter for type than for the colour.

The significance of the trends is measured, as previously, in terms of the residuals between medians (see Table 1). For the gradients towards filaments, the difference of $\gtrsim 6\sigma$ is found between the most extreme, both mass and sSFR, bins, while it drops to $\sim$2–3σ between the intermediate and lowest bins. For the gradients towards walls, the deviation between the most extreme bins is $\sim$10 and 4σ for mass and sSFR bins, respectively, while there is only a little to no difference between intermediate and lowest stellar mass and sSFR bins, respectively. The gradients are slightly less significant than in the GAMA measurements, most likely due to the low numbers of galaxies per individual bins in HORIZON-AGN, but qualitatively similar as in GAMA.

6 THE RELATIVE IMPACT OF DENSITY

Let us now address the following questions: what is the specific role of the geometry of the large-scale environment in establishing mass and type/colour large-scale gradients? Are these gradients driven solely by density, or does the large-scale anisotropy of the cosmic web provide a specific signature?

A key ingredient in answering these questions is the choice of the scale at which the density is inferred. The properties of galaxies at a given redshift are naturally a signature of their past light-cone. This light-cone in turn correlates with the galaxy's environment: the larger the scale is, the longer the look-back time one must consider, the more integrated the net effect of this environment. This past environment accounts for the total accreted mass of the galaxy, but may also impact the geometry of the accretion history and more generally other galactic properties such as its star formation efficiency, its colour or its spin. At small scales, the density correlates with the most recent and stochastic processes, while going to larger scales allows taking the integrated hence smoother history of galaxies into account. Since this study is concerned about the statistical impact of the large-scale structure on galaxies, it is natural to consider scales large enough to average out local recent events they may have encountered, such as binary interactions, mergers and outflows. Therefore in the discussion below, the density is computed at the scale of 8 Mpc, the 'smallest' scale at which the effect of the anisotropic large-scale tides can be detected.

In practice, in order to try to disentangle the effect of density from that of the anisotropic large-scale tides, the following reshuffling method (e.g. Malavasi et al. 2017) is adopted. For mass gradients, 10 equipopulated density bins are constructed and in each of them the stellar masses of galaxies are randomly permuted. By construction, the underlying mass-density relation is preserved, but this procedure randomizes the relation between the stellar mass and the distance to the filament or the wall. For the type/colour gradients, in each of 10 equipopulated density bins, 10 equipopulated stellar mass bins are constructed. Within each of such bins, $u - r$ colour of galaxies are randomly permuted. Thus by construction, this preserves the underlying colour-(mass)-density relation, but breaks the relation between the colour/type and the distance to the particular environment, the filament or wall.

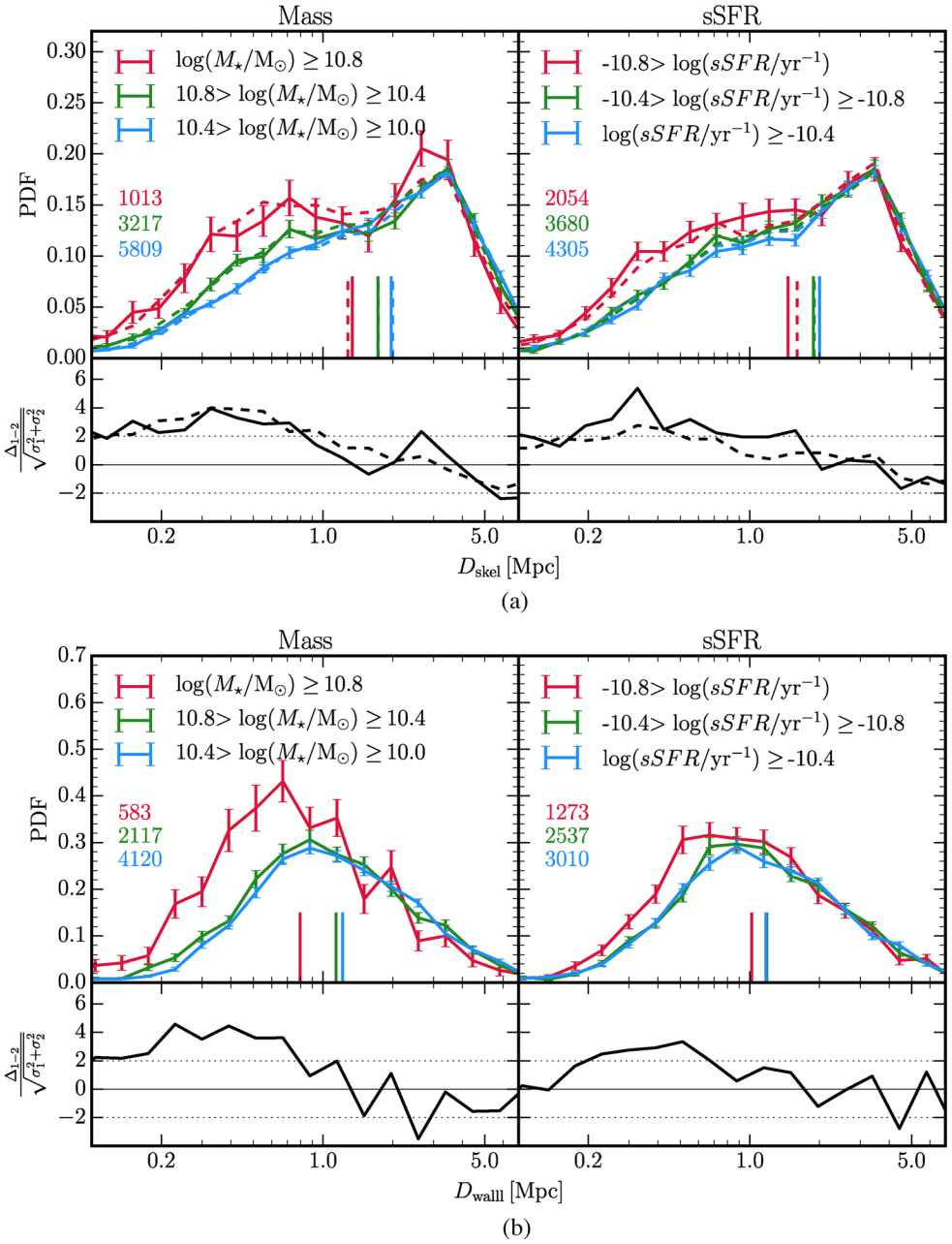

Figure 11. *Top rows:* Differential distributions of the distances as a function of stellar mass (left-hand panels) and sSFR (right-hand panels) for galaxies in HORIZON-AGN. To minimize the contribution of nodes and filaments to the measured signal, galaxies located closer to a node than 3.5 Mpc and closer to a filament than 1 Mpc are removed from the analysis. The vertical lines indicate the medians of the distributions (see Table 2 for the numerical values). Numbers of galaxies in different considered bins are indicated in each panel. There is mass and sSFR segregation of galaxies with respect to both filaments and walls: more massive and less star-forming galaxies tend to be preferentially located closer to the cores of filaments and walls compared to their lower-mass and more star-forming counterparts, respectively. These results are in qualitative agreement with the measurements in GAMA. *Bottom rows:* Residuals in units of σ between the two most extreme mass and sSFR bins, $\log(M_\star/\mathrm{M}_\odot) \geq 10.8$ and $10.4 > \log(M_\star/\mathrm{M}_\odot) \geq 10$ on the left-hand panel and $-10.8 > \log(\mathrm{sSFR/yr}^{-1})$ and $\log(\mathrm{sSFR/yr}^{-1}) \geq -10.4$ on the right-hand panel, respectively. (a) Differential distributions of the distances to the nearest filament, $D_{\rm skel}$. (b) Differential distributions of the distances to the nearest wall, $D_{\rm wall}$.

In order to account for the variation of the density through the survey, the density contrast, defined as $1 + \delta = n/n(z)$, where $n(z)$ corresponds to the mean redshift-dependent number density, is used in logarithmic bins. The number density n is computed in the Gaussian kernel and every time five reshuffled samples are constructed.

In Fig. 12(a), the mass and type gradients towards filaments, as measured in GAMA and previously shown in Figs 6 and 7, are compared with the outcome of the reshuffling technique. The original signal is found to be substantially reduced after the reshuffling of masses and colours of galaxies. For the mass gradients, the deviation between the most extreme bins before reshuffling exceeds 3σ, while after the reshuffling, the signal gets reduced, with typical deviations of $\sim 1\sigma$. The original signal for the type/colour gradients is weaker than in the case of the mass gradients, however it is similarly nearly cancelled out once the reshuffling method is

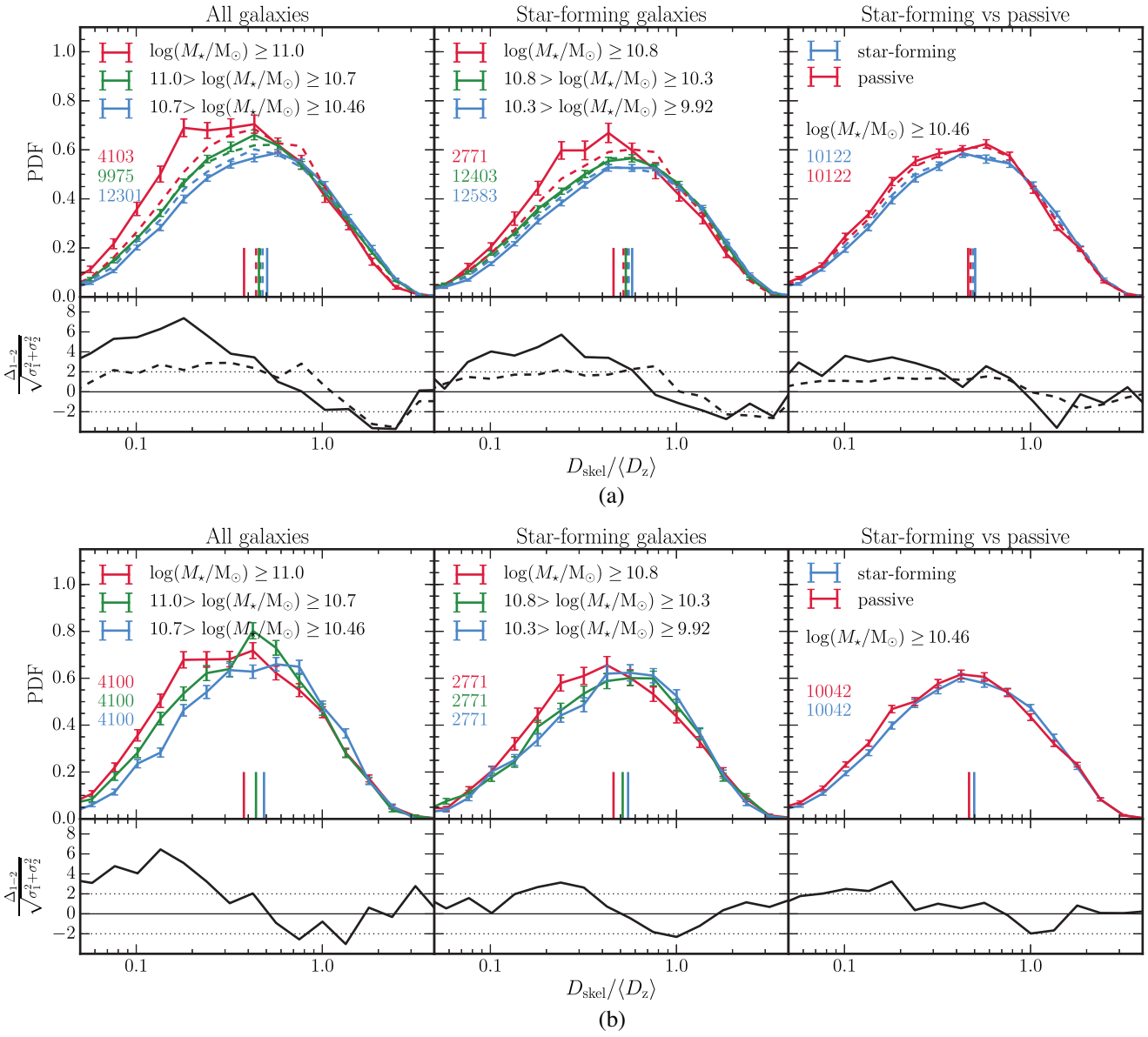

Figure 12. *Top rows:* Differential distributions of the normalized distances to the nearest filament, $D_{\rm skel}$ as a function of stellar mass of the entire galaxy population (left-hand panels), for star-forming galaxies only (middle panels) and as a function of galaxy's type (right-hand panels) with reshuffling (Figure a) and with density-matched samples (Figure b). In Figure (a), the distributions before applying the reshuffling method (solid lines) are compared to the results after the reshuffling (dashed lines). Figure (b) illustrates the distributions for the galaxy samples that are matched so that their density distributions are the same (see the text for details on the matching). The density estimators used in both the reshuffling and density matching corresponds to the (large-scale) density computed in the Gaussian kernel at the scale of 8 Mpc. As previously, the contribution of nodes to the measured signal is minimized. The numerical values of medians, shown as vertical lines, are listed in Table 3. The two methods yield qualitatively similar result: on the one hand when the large-scale density is used in reshuffling, the signal is reduced (dashed lines, Figure a) suggesting that the measured gradients (solid lines, Figure a) are not driven by the density at this scale, on the other hand, the gradients are measured within the samples that are matched in density at large scale. *Bottom rows:* Residuals in units of σ between the highest and lowest mass bins (left-hand and middle panels) and between the star-forming and passive galaxies (right-hand panels). (a) Reshuffling. (b) Density matching.

applied. The values of medians of the distributions after the reshuffling can be found in Table 3. Qualitatively similar behaviour is obtained for the gradients towards walls (not shown here). The analysis in HORIZON-AGN provides a qualitative support for these results. In Appendix D2, Fig. D1(a), the same reshuffling method is applied to simulated galaxies. The density used for this test is computed in the Gaussian kernel at 5 Mpc. This scale corresponds to the ∼1.5× mean inter-galaxy separation in HORIZON-AGN, consistently with the GAMA data.

Alternatively, to assess the impact of the density on the measured gradients within the cosmic web, one may want to use density matching. The purpose of this method is to construct mass- and colour-density matched samples, whereby galaxies with different masses and/or colours have similar density distributions, in order to make sure that the measured properties are not driven by their differences (see Appendix A2 for details on the matching technique). As shown in Fig. 12(b), the main result on the density-matching technique leads to the same conclusions as the reshuffling method.

Table 3. Medians for the PDFs displayed in Fig. 12: large-scale density

	Selection[a]	Bin	Median[b]		
			Original[c]	$D_{\rm skel}/\langle D_{\rm z}\rangle$ reshuffling[d]	Matching[e]
Masses	All galaxies	$\log(M_\star/{\rm M}_\odot) \geq 11$	0.379 ± 0.009	0.441 ± 0.009	0.379 ± 0.01
		$11 > \log(M_\star/{\rm M}_\odot) \geq 10.7$	0.456 ± 0.007	0.463 ± 0.006	0.44 ± 0.009
		$10.7 > \log(M_\star/{\rm M}_\odot) \geq 10.46$	0.505 ± 0.007	0.475 ± 0.006	0.486 ± 0.01
	SF galaxies	$\log(M_\star/{\rm M}_\odot) \geq 11$	0.459 ± 0.01	0.541 ± 0.015	0.459 ± 0.011
		$11 > \log(M_\star/{\rm M}_\odot) \geq 10.4$	0.534 ± 0.007	0.543 ± 0.007	0.514 ± 0.012
		$10.4 > \log(M_\star/{\rm M}_\odot) \geq 9.92$	0.578 ± 0.007	0.552 ± 0.007	0.549 ± 0.012
Types	SF versus passive[f]	Star-forming	0.503 ± 0.007	0.491 ± 0.007	0.498 ± 0.007
		Passive	0.462 ± 0.007	0.476 ± 0.007	0.467 ± 0.006

Notes. [a]Panels of Fig. 12.
[b]Medians of distributions as indicated in Fig. 12 by vertical lines; errors are computed as in Table 1.
[c]As in Table 1 for $D_{\rm skel}/\langle D_z\rangle$.
[d]Reshuffling is done in bins of density computed at 8 Mpc (see the text for details).
[e]Medians for the density-matched sample, where the density considered is computed at 8 Mpc.
[f]Only galaxies with stellar masses $\log(M_\star/{\rm M}_\odot) \geq 10.46$ are considered.

After matching galaxy populations in the large-scale density, mass and type gradients towards filaments and walls are still detected, suggesting that beyond the density, large-scale structures of the cosmic web do impact these galactic properties.

7 DISCUSSION

Let us first discuss the observational findings of the previous section in the framework of existing work (Section 7.1) and then focus on a recent extension of anisotropic excursion set which is developed in the companion paper (Section 7.2). The latter will allow us to explain why colour gradients prevail at fixed density.

7.1 Cosmic web metric: expected impact on galaxy evolution

In the current framework for galaxy formation, in which galaxies reside in extended dark matter haloes, it is quite natural to split the environment into the *local* environment, defined by the dark matter halo and the *global* large-scale anisotropic environment, encompassing the scale beyond the halo's virial radius. The anisotropy of the cosmic web is already a direct manifestation of the generic anisotropic nature of gravitational collapse on larger scales. It provides the embedding in which dark haloes and galaxies grow via accretion, which will act upon them via the combined effect of tides, the channeling of gas along preferred directions and angular momentum advection on to forming galaxies.

The observations and simulations presented in Sections 4, 5 and 6 provide a general support for this scenario. While rich clusters and massive groups are known to be environments which induce major galaxy transformations, the red fraction analysis presented in Section 4.1 (Fig. 5) reveals that the fraction of passive galaxies in the filaments starts to increase several Mpc away from the nodes and peaks in the nodes. This gradual increase suggests that some 'pre-processing' already happens before the galaxies reach the virial radius of massive haloes and fall into groups or clusters (e.g. Porter et al. 2008; Martínez et al. 2016). The above-mentioned morphological transformation of elliptical-to-spiral ratio when getting closer to the filaments (see also Kuutma et al. 2017) can be interpreted as the result of mergers transforming spirals into passive elliptical galaxies along the filaments when migrating towards nodes as suggested by theory and simulations (Codis et al. 2012; Dubois et al. 2014). These findings show that filamentary regions, corresponding to intermediate densities, are important environments for galaxy transformation. This is also confirmed by the segregation found in Sections 4.2 (Figs 6 and 7). More massive and/or passive galaxies are found closer to the core of filaments than their less massive and/or star-forming counterparts. These differential mass gradients persist among the star-forming population alone. In addition to mass segregation, star-forming galaxies show a gradual evolution in their star formation activity (see Fig. 8). They are bluer than average at large distances from filaments ($D_{\rm skel} \gtrsim 5$ Mpc), in a 'steady state' with no apparent evolution in star formation activity at intermediate distances ($0.5 \leq D_{\rm skel} \leq 5$ Mpc) and they show signs of decreased star formation efficiency near the core of the filaments ($D_{\rm skel} \lesssim 0.5$ Mpc). These results are in line with the picture where on the one hand more massive/passive galaxies lay in the core of filaments and merge while drifting towards the nodes of the cosmic web. On the other hand, the low mass/star-forming galaxies tend to be preferentially located in the outskirts of filaments, a vorticity-rich regions (Laigle et al. 2015), where galaxies acquire both their angular momentum (leading to a spin parallel to the filaments) and their stellar mass via essentially smooth accretion (Dubois et al. 2012b; Welker et al. 2017, also relying on HORIZON-AGN). The steady state of star-formation in these regions can reflect the right balance between the consumption and refuelling of the gas reservoir by the cold gas controlled by their surrounding filamentary structure (as shown by Codis et al. 2015, following Pichon et al. 2011, the outskirts of filaments are the loci of most efficient helicoidal infall of cold gas). This may not be true anymore when galaxies fall in the core of the filaments. The decline of star formation activity can, in part, be due to the higher merger rate but also due to a quenching process such as strangulation, where the supply of cold gas is halted (Peng, Maiolino & Cochrane 2015). It could also find its origin in the cosmic web detachment (Aragon-Calvo et al. 2016), where the turbulent regions inside filaments prevent galaxies to stay connected to their filamentary flows and thus to replenish their gas reservoir.

7.2 Link with excursion set theory

The distinct transverse gradients found for mass, density and type or colour may also be understood within the framework of conditional excursion set theory. Qualitatively, the spatial variation of the (traceless part of the) tidal tensor in the vicinity of filaments will

delay infall on to galaxies, which will impact differentially galactic colour (at fixed mass), provided accretion can be reasonably converted into star formation efficiency.

7.2.1 *Connecting gradients to constrained excursion set*

The companion paper (Musso et al. 2017) revisits excursion set theory subject to conditioning the excursion to the vicinity of a filament. In a nutshell, the main idea of excursion set theory is to compute the statistical properties of the initial (over)density – a stochastic variable – enclosed within spheres of radius R, the scale which, through the spherical collapse model, can be related to the final mass of the object (should the density within the sphere pass the threshold for collapse). Increasing the radius of the sphere provides us with a proxy for 'evolution' (larger sphere, larger mass, smaller variance, later formation time) *and* a measure of the impact of the environment (different sensitivity to tides for different, larger, spheres). The expectations associated with this stochastic variable can be re-computed subject to the tides imposed by larger scale structures, which are best captured by the geometry of a filament-saddle point, $\mathcal{S}$, providing the local natural 'metric' for a filament (Codis et al. 2015). These large-scale tides will induce distinct weighting in the conditional PDF(δ, $\partial_R\delta|\mathcal{S}$) for the overdensity δ, and its successive derivatives with respect to scale, $\partial_R\delta$ etc. (so as to focus on collapsed accreting regions). Indeed, the saddle will shift not only the mean expectation of the PDFs but also importantly their co-variances (see Musso et al. 2017, for details). The derived expected (dark matter) mean density $\rho(r,\theta,\phi)$, Press-Schechter mass $M(r,\theta,\phi)$ and typical accretion rate $\dot{M}(r,\theta,\phi)$ then become explicit *distinct* functions of distance r and relative orientation to the closest (oriented) saddle point. Within this model, it follows that the orientation of the mass, density and accretion rate gradients differ. The misalignment arises because the various fields weight differently the constrained tides, which will physically e.g. delay infall, and technically involve different moments of the aforementioned conditional PDF (see Appendix E for more quantitative information on contour misalignment). This is shown in Fig. 13, which displays a typical longitudinal cross-section of those three maps in the frame of the saddle (with the filament along the Oz axis) in Lagrangian space.[5]

This line of argument explains environmentally driven differential gradients, yet there is still a stretch to connect it to the observed gradients. While there is no obvious consensus on the detailed effect of large-scale (dark matter) accretion on to the colour or star formation of galaxies at fixed mass and density, one can expect that the stronger the accretion, the stronger the AGN feedback, the stronger the quenching. Should this (reasonable) scaling hold true, the net effect in terms of gradients would be that colour gradients differ from mass and density ones. This is qualitatively consistent with the findings of this paper.

[5] This companion paper does not capture the strongly non-linear process of dynamical friction of sub clumps within dark haloes, nor strong deviations from spherical collapse. We refer to Hahn et al. (2009), which captures the effect on satellite galaxies, and to Ludlow, Borzyszkowski & Porciani (2014), Castorina et al. (2016) and Borzyszkowski et al. (2017) which study the effect of the local shear on haloes forming in filamentary structures. This requires adopting a threshold for collapse that depends explicitly on the local shear. The shear-dependent part of the critical density (and its derivative) correlates with the shear of the saddle, and introduces an additional anisotropic effect on top of the change of mean values and variances of density and slope.

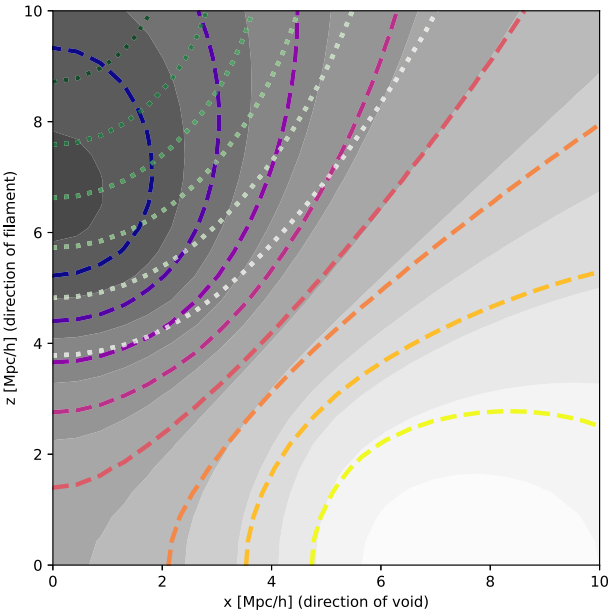

Figure 13. Isocontours of constant typical redshift $z = 0$ mean density (filled contours), mass (dotted lines) and accretion rate (dashed lines) in the frame of a filament (along the Oz axis) in Lagrangian space (initial conditions) from low (light colours) to high values (dark colours). The saddle is at coordinate (0,0) while the induced peak and void are at coordinates (0,±7) and (±8,0) h^{-1}Mpc, respectively. As argued in the main text, this figure shows that the contours, hence the gradients of the three fields, are not parallel (the contours cross). The choice of scale sets the units on the x- and z-axis (chosen here to be 5 h^{-1}Mpc, while the mass and accretion rates are computed for a local smoothing of 0.5 h^{-1}Mpc). At lower redshift/smaller scales, one expects the non-linear convergence of the flow towards the filament to bring those contours together, aligning the gradients (see Fig. 14).

7.2.2 *Gradient alignments on smaller non-linear scales*

The above-presented Lagrangian theory clearly applies only on sufficiently large scales so that dynamical evolution has not driven the large-scale flow too far from its initial configuration. On smaller scales, one would expect the same line of argument to operate in the frame set by the saddle smoothed on the corresponding scale, but with one extra caveat: the increased level of non-linearity will have compressed the local filament transversally and stretched it longitudinally, following the generic kinetic flow measured in N-body simulation (e.g. Sousbie et al. 2008a), or predicted at the level of the Zel'dovich approximation (Codis et al. 2015).

Consequently, the contours of constant dark matter density ρ, typical dark halo mass M and typical relative accretion rate $\dot{M}/M$ in the frame of the saddle shown in Fig. 13 will be driven more parallel to each other, hence the difference in the orientation of the density, mass and accretion gradient will become smaller and smaller as one considers smaller scales, and/or more non-linear dynamics (see Fig. 14). As colour gradient at fixed mass, and mass gradient at fixed density towards filaments originate from this initial misalignment, it should come as no surprise that as one probes smaller scales, such relative gradients disappear. When considering statistical expectations concerned with anisotropy (delayed accretion, acquisition of angular momentum, etc.), the net effect of past interactions should first be considered on the largest significant scale, beyond which the universe becomes isotropic. Conversely, the level of stochasticity should increase significantly on smaller scales, where one must

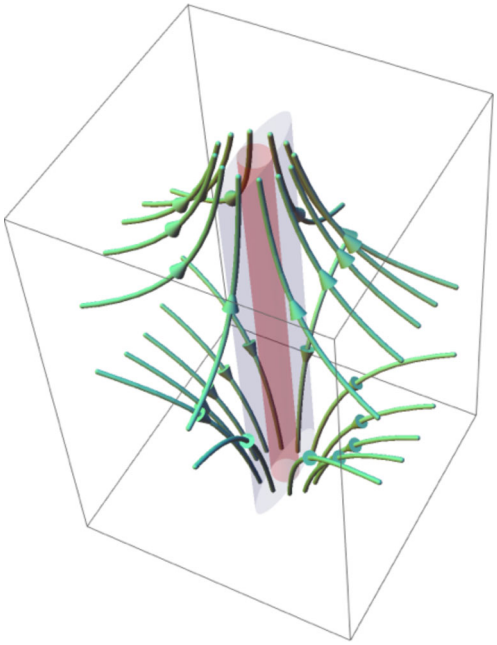

Figure 14. Illustration of the Zel'dovich flow (green arrows) in the vicinity of a filament (red cylinder) embedded in a wall (purple flattened cylinder), with filament saddle at the centre. The non-linear evolution operating more strongly on smaller scales will advect the contours presented in Fig. 13 along the green arrows, bringing them more parallel to each other. Consequently at these smaller scales, the mass and accretion gradients do not differ significantly from the density gradients. See Codis et al. (2015) and Musso et al. (2017) for more details.

account for, e.g. the configuration of the last merger event, or the last fly-by. Such a scenario is indeed supported by our findings in both GAMA and HORIZON-AGN, presented in Appendices C and D2, Figs C1 and D1, respectively, whereby the use of the small-scale density tracer does not allow us to disentangle between the effects of the local density and that of cosmic web, suggesting that at such scale, they are closely correlated through the small-scale processes.

7.2.3 Relationship to wall gradients

When measured relative to the walls, galaxy properties are found to exhibit the same trends as for filaments, in that more massive and/or quiescent galaxies are found closer to the walls than their low mass and/or star-forming counterparts. This result is again in qualitative agreement with the idea of walls being, together with the filaments, the large-scale interference patterns of primordial fluctuations capable of inducing anisotropic boost in overdensity together with the corresponding tides, and consequently imprinting their geometry in the measured properties of galaxies. The gradients measured for walls have the same origin as those inducing the differential gradients near the filament-type saddles, but are sourced by the geometry of the tides near the wall-type saddles (Codis et al. 2015, Appendix B). The main difference between the two saddles lies in the transverse curvatures, which is steeper for wall-type saddles than for filament-type saddles (when considering the mean, eigenvolume weighted, eigenvalues of the curvature tensor with the relevant signatures) leading to weaker differences between the different gradients when considering walls. This is consistent with the findings of Section 4.3.

In closing, note that the (resp. Eulerian and Lagrangian) interpretations presented in Sections 7.1 and 7.2 are complementary, but fall short in explaining in details the origin of quenching. Nevertheless, in view of both observation and theory, the cosmic web metric appears as a natural framework to understand galaxy formation beyond stellar mass and local density.

8 SUMMARY AND CONCLUSIONS

This paper studies the impact of the large-scale environment on the properties of galaxies, such as their stellar mass, dust corrected $u - r$ colour and sSFR. The discrete persistent structure extractor (DisPerSE) was used to identify the peaks, filaments and walls in the large-scale distribution of galaxies as captured by the GAMA survey. The principal findings are the following.

(i) *Mass segregation.* Galaxies are found to segregate by stellar mass, such that more massive galaxies are preferentially located closer to the cores of filaments than their lower mass counterparts. This mass segregation persists among the star-forming population. Similar mass gradients are seen with respect to walls in that galaxies with higher stellar mass tend to be found closer to the walls compared to galaxies with lower mass and persisting even when star-forming population of galaxies is considered alone.

(ii) *Type/colour segregation.* Galaxies are found to segregate by type/colour, with respect to both filaments and walls, such that passive galaxies are preferentially located closer to the cores of filaments or walls than their star-forming counterparts.

(iii) *Red fractions.* The fraction of passive galaxies increases with both decreasing distance to the filament and to the node, i.e. at fixed distance to the node, the relative number of passive galaxies (with respect to the entire population) increases as the distance to the filament decreases and similarly, at a given distance to the filament, this number increases with decreasing distance to the node.

(iv) *Star formation activity.* Star-forming galaxies are found to carry an imprint of large-scale environment as well. Their dust corrected $u - r$ and sSFR are found to be more enhanced and reduced, respectively, in the vicinity of the filaments compared to their outskirts.

(v) *Consistency with cosmological simulations.* All the found gradients are consistent with the analysis of the HORIZON-AGN 'full physics' hydrodynamical simulation. This agreement suggests that what drives the gradients is captured by the implemented physics.

(vi) *Connection to excursion set theory.* The origin of the distinct gradients can be qualitatively explained via conditional excursion set theory subject to filamentary tides (Musso et al. 2017).

This work has focused on filaments, nodes and in somewhat lesser details on walls. Similar observational results were recently reported at high redshift by using the cosmic web filamentary structures in the VIPERS spectroscopic survey (Malavasi et al. 2017) and while using projected filaments in photometric redshift slices in the COSMOS field (Laigle et al. 2017). These observations are of intrinsic interest as a signature of galactic assembly; they also comfort theoretical expectations which point towards distinct gradients for colour, mass and density with respect to the cosmic web. The tides of the large-scale environment play a significant specific role in the evolution of galaxies, and are imprinted in their integrated physical properties, which vary as a function of scale and distance to the different components of the cosmic web in a manner which is specific to each observable.

These observations motivate a theory which eventually should integrate the anisotropy of the cosmic web as an essential ingredient to (i) describe jointly the dynamics and physics of galaxies, (ii) explain galactic morphological diversity, and (iii) mitigate intrinsic alignment in upcoming lensing dark energy experiments, once a proper modelling of the mapping between galaxies and their haloes (allowing e.g. to convert the DM accretion rate into colour of galaxy) becomes available.

Future large-scale spectrographs on 8 metre class telescopes (MOONS;[6] Cirasuolo et al. 2014; Cirasuolo & MOONS Consortium 2016, PFS;[7] Sugai et al. 2015) or space missions (WFIRST;[8] Spergel et al. 2013, 2015, and Euclid;[9] Laureijs et al. 2011, the deep survey for the latter) will extend the current analysis at higher redshift ($z \geq 1$) with similar samplings, allowing us to explore the role of the environment near the peak of the cosmic star formation history, an epoch where the connectivity between the LSS and galaxies is expected to be even tighter, with ubiquitous cold streams. Tomography of the Lyman-α forest with PFS, MOONS, ELT-HARMONI (Thatte et al. 2010) tracing the intergalactic medium will make the study of the link between galaxies and this large-scale gas reservoir possible.

ACKNOWLEDGEMENTS

The authors thank the anonymous referee for suggestions and comments that helped to improve the presentation of the paper. This research is carried out within the framework of the Spin(e) collaboration (ANR-13-BS05-0005, http://cosmicorigin.org). We thank the members of this collaboration for numerous discussions. The HORIZON-AGN simulation was post processed on the Horizon Cluster hosted by Institut d'Astrophysique de Paris. We thank S. Rouberol for running it smoothly for us. GAMA is a joint European-Australasian project based around a spectroscopic campaign using the Anglo-Australian Telescope. The GAMA input catalogue is based on the data taken from the Sloan Digital Sky Survey and the UKIRT Infrared Deep Sky Survey. Complementary imaging of the GAMA regions is being obtained by a number of independent survey programmes including GALEX MIS, VST KiDS, VISTA VIKING, WISE, Herschel-ATLAS, GMRT and ASKAP providing UV to radio coverage. GAMA is funded by the STFC (UK), the ARC (Australia), the AAO, and the participating institutions. The GAMA web site is http://www.gama-survey.org/. The VISTA VIKING data used in this paper are based on observations made with ESO Telescopes at the La Silla Paranal Observatory under programme ID 179.A-2004. CC acknowledges support through the ILP PhD thesis fellowship. CL is supported by a Beecroft Fellowship.

REFERENCES

Alpaslan M. et al., 2015, MNRAS, 451, 3249
Alpaslan M. et al., 2016, MNRAS, 457, 2287
Andrae R., Jahnke K., 2011, MNRAS, 418, 2014
Aragon-Calvo M. A., Yang L. F., 2014, MNRAS, 440, L46
Aragón-Calvo M. A., Jones B. J. T., van de Weygaert R., van der Hulst J. M., 2007a, A&A, 474, 315
Aragón-Calvo M. A., van de Weygaert R., Jones B. J. T., van der Hulst J. M., 2007b, ApJ, 655, L5
Aragón-Calvo M. A., van de Weygaert R., Jones B. J. T., 2010, MNRAS, 408, 2163
Aragon-Calvo M. A., Neyrinck M. C., Silk J., 2016, preprint (arXiv:1607.07881)
Arnouts S., Cristiani S., Moscardini L., Matarrese S., Lucchin F., Fontana A., Giallongo E., 1999, MNRAS, 310, 540
Aubert D., Pichon C., Colombi S., 2004, MNRAS, 352, 376
Baldry I. K., Balogh M. L., Bower R. G., Glazebrook K., Nichol R. C., Bamford S. P., Budavari T., 2006, MNRAS, 373, 469
Bamford S. P. et al., 2009, MNRAS, 393, 1324
Barnes J., Efstathiou G., 1987, ApJ, 319, 575
Benítez-Llambay A., Navarro J. F., Abadi M. G., Gottlöber S., Yepes G., Hoffman Y., Steinmetz M., 2013, ApJ, 763, L41
Beygu B., Kreckel K., van der Hulst J. M., Jarrett T. H., Peletier R., van de Weygaert R., van Gorkom J. H., Aragon-Calvo M. A., 2016, MNRAS, 458, 394
Blanton M. R. et al., 2003, ApJ, 594, 186
Blumenthal G. R., Faber S. M., Primack J. R., Rees M. J., 1984, Nature, 311, 517
Bond J. R., Myers S. T., 1996, ApJS, 103, 1
Bond J. R., Cole S., Efstathiou G., Kaiser N., 1991, ApJ, 379, 440
Bond J. R., Kofman L., Pogosyan D., 1996, Nature, 380, 603
Bond N. A., Strauss M. A., Cen R., 2010a, MNRAS, 406, 1609
Bond N. A., Strauss M. A., Cen R., 2010b, MNRAS, 409, 156
Borzyszkowski M., Porciani C., Romano-Diaz E., Garaldi E., 2017, MNRAS, 469, 594
Bruzual G., Charlot S., 2003, MNRAS, 344, 1000
Castorina E., Paranjape A., Hahn O., Sheth R. K., 2016, preprint (arXiv:1611.03619)
Cautun M. C., van de Weygaert R., 2011, Astrophysics Source Code Library, record ascl:1105.003
Cervantes-Sodi B., Hernandez X., Park C., 2010, MNRAS, 402, 1807
Chen Y.-C. et al., 2017, MNRAS, 466, 1880
Cirasuolo M. et al., 2014, Proc. SPIE, 9147, 91470N
Cirasuolo M., MOONS Consortium 2016, in Skillen I., Barcells M., Trager S., eds, ASP Conf. Ser. Vol. 507, Multi-Object Spectroscopy in the Next Decade: Big Questions, Large Surveys, and Wide Fields. Astron. Soc. Pac., San Francisco, p. 109
Codis S., Pichon C., Devriendt J., Slyz A., Pogosyan D., Dubois Y., Sousbie T., 2012, MNRAS, 427, 3320
Codis S., Pichon C., Pogosyan D., 2015, MNRAS, 452, 3369
Colless M., Dalton G., Maddox S., Sutherland W., Norberg P., Cole S., Bland-Hawthorn J., 2001, MNRAS, 328, 1039
Colombi S., Pogosyan D., Souradeep T., 2000, Phys. Rev. Lett., 85, 5515
Davis M., Efstathiou G., Frenk C. S., White S. D. M., 1985, ApJ, 292, 371
De Lapparent V., Geller M. J., Huchra J. P., 1986, ApJ, 302, L1
Doroshkevich A. G., 1970, Astrofizika, 6, 581
Dressler A., 1980, ApJ, 236, 351
Dressler A. et al., 1997, ApJ, 490, 577
Driver S. P. et al., 2009, Astron. Geophys., 50, 5.12
Driver S. P., Hill D. T., Kelvin L. S., Robotham A. S. G., Liske J., Norberg P., Baldry I. K., 2011, MNRAS, 413, 971
Driver S. P. et al., 2016, MNRAS, 455, 3911
Dubois Y., Devriendt J., Slyz A., Teyssier R., 2012a, MNRAS, 420, 2662
Dubois Y., Pichon C., Haehnelt M., Kimm T., Slyz A., Devriendt J., Pogosyan D., 2012b, MNRAS, 423, 3616
Dubois Y. et al., 2014, MNRAS, 444, 1453
Eardley E., Peacock J. A., McNaught-Roberts T., Heymans C., Norberg P., Alpaslan M., Baldry, 2015, MNRAS, 448, 3665
Efstathiou G., Jones B. J. T., 1979, MNRAS, 186, 133
Efstathiou G., Frenk C. S., White S. D. M., Davis M., 1988, MNRAS, 235, 715
Eke V. R. et al., 2004, MNRAS, 348, 866
Forero-Romero J. E., Hoffman Y., Gottlöber S., Klypin A., Yepes G., 2009, MNRAS, 396, 1815
Gay C., Pichon C., Le Borgne D., Teyssier R., Sousbie T., Devriendt J., 2010, MNRAS, 404, 1801
Geller M. J., Huchra J. P., 1989, Science, 246, 897

[6] Multi-Object Optical and Near-infrared Spectrograph.
[7] Prime Focus Spectrograph; http://pfs.ipmu.jp/
[8] Wide-Field Infrared Survey Telescope; http://wfirst.gsfc.nasa.gov
[9] http://sci.esa.int/euclid/, http://www.euclid-ec.org

Goto T., Yamauchi C., Fujita Y., Okamura S., Sekiguchi M., Smail I., Bernardi M., Gomez P. L., 2003, MNRAS, 346, 601
Guo Q., Tempel E., Libeskind N. I., 2015, ApJ, 800, 112
Haardt F., Madau P., 1996, ApJ, 461, 20
Hahn O., Porciani C., Carollo C. M., Dekel A., 2007a, MNRAS, 375, 489
Hahn O., Carollo C. M., Porciani C., Dekel A., 2007b, MNRAS, 381, 41
Hahn O., Porciani C., Dekel A., Carollo C. M., 2009, MNRAS, 398, 1742
Hahn O., Angulo R. E., Abel T., 2015, MNRAS, 454, 3920
Hashimoto Y., Oemler Jr A., Lin H., Tucker D. L., 1998, ApJ, 499, 589
Heavens A., Peacock J., 1988, MNRAS, 232, 339
Hopkins A. M. et al., 2013, MNRAS, 430, 2047
Ilbert O. et al., 2006, A&A, 457, 841
Jackson J. C., 1972, MNRAS, 156, 1P
Jõeveer M., Einasto J., Tago E., 1978, MNRAS, 185, 357
Jones B. J. T., Efstathiou G., 1979, MNRAS, 189, 27
Jones B. J. T., van de Weygaert R., Aragón-Calvo M. A., 2010, MNRAS, 408, 897
Kaiser N., 1984, ApJ, 284, L9
Kaiser N., 1987, MNRAS, 227, 1
Kauffmann G., White S. D. M., Heckman T. M., Ménard B., Brinchmann J., Charlot S., Tremonti C., Brinkmann J., 2004, MNRAS, 353, 713
Kleiner D., Pimbblet K. A., Jones D. H., Koribalski B. S., Serra P., 2017, MNRAS, 466, 4692
Komatsu E. et al., 2011, ApJS, 192, 18
Kuutma T., Tamm A., Tempel E., 2017, A&A, 600, L6
Laigle C. et al., 2015, MNRAS, 446, 2744
Laigle C. et al., 2017, preprint (arXiv:1702.08810)
Laureijs R. et al., 2011, preprint (arXiv:1110.3193)
Lee J., 2004, ApJ, 614, L1
Lee J., Erdogdu P., 2007, ApJ, 671, 1248
Lewis I. et al., 2002, MNRAS, 334, 673
Libeskind N. I., Hoffman Y., Knebe A., Steinmetz M., Gottlöber S., Metuki O., Yepes G., 2012, MNRAS, 421, L137
Libeskind N. I. et al., 2017, preprint (arXiv:1705.03021)
Liske J. et al., 2015, MNRAS, 452, 2087
Ludlow A. D., Borzyszkowski M., Porciani C., 2014, MNRAS, 445, 4110
Malavasi N. et al., 2017, MNRAS, 465, 3817
Martínez H. J., Muriel H., Coenda V., 2016, MNRAS, 455, 127
Merson A. I. et al., 2013, MNRAS, 429, 556
Mo H., van den Bosch F. C., White S., 2010, Galaxy Formation and Evolution. Cambridge Univ. Press, Cmabridge
Musso M., Cadiou C., Pichon C., Codis S., Dubois Y., 2017, preprint (arXiv:1709.00834)
Navarro J. F., Abadi M. G., Steinmetz M., 2004, ApJ, 613, L41
Novikov D., Colombi S., Doré O., 2006, MNRAS, 366, 1201
Pahwa I. et al., 2016, MNRAS, 457, 695
Paz D. J., Stasyszyn F., Padilla N. D., 2008, MNRAS, 389, 1127
Peebles P. J. E., 1969, ApJ, 155, 393
Peng Y., Maiolino R., Cochrane R., 2015, Nature, 521, 192
Pichon C., Pogosyan D., Kimm T., Slyz A., Devriendt J., Dubois Y., 2011, MNRAS, 418, 2493
Planck Collaboration XIII, 2016, A&A, 594, A13
Pogosyan D., Bond J. R., Kofman L., Wadsley J., 1996, in American Astronomical Society Meeting Abstracts, p. 1289
Pogosyan D., Pichon C., Gay C., Prunet S., Cardoso J. F., Sousbie T., Colombi S., 2009, MNRAS, 396, 635
Porciani C., Dekel A., Hoffman Y., 2002a, MNRAS, 332, 325
Porciani C., Dekel A., Hoffman Y., 2002b, MNRAS, 332, 339
Porter S. C., Raychaudhury S., Pimbblet K. A., Drinkwater M. J., 2008, MNRAS, 388, 1152
Postman M., Geller M. J., 1984, ApJ, 281, 95
Robotham A. S. G. et al., 2011, MNRAS, 416, 2640
Robotham A. S. G. et al., 2013, MNRAS, 431, 167
Rojas R. R., Vogeley M. S., Hoyle F., Brinkmann J., 2004, ApJ, 617, 50
Schaap W. E., van de Weygaert R., 2000, A&A, 363, L29
Schmidt M., 1959, ApJ, 129, 243
Shi F. et al., 2016, ApJ, 833, 241
Sousbie T., 2011, MNRAS, 414, 350
Sousbie T., Pichon C., Colombi S., Novikov D., Pogosyan D., 2008a, MNRAS, 383, 1655
Sousbie T., Pichon C., Courtois H., Colombi S., Novikov D., 2008b, ApJ, 672, L1
Sousbie T., Pichon C., Kawahara H., 2011, MNRAS, 414, 384
Spergel D. et al., 2013, preprint (arXiv:1305.5422)
Spergel D. et al., 2015, preprint (arXiv:1503.03757)
Stewart K. R., Brooks A. M., Bullock J. S., Maller A. H., Diemand J., Wadsley J., Moustakas L. A., 2013, ApJ, 769, 74
Subba Rao M. U., Aragón-Calvo M. A., Chen H. W., Quashnock J. M., Szalay A. S., York D. G., 2008, New J. Phys., 10, 125015
Sugai H. et al., 2015, J. Astron. Telescopes Instrum. Syst., 1, 035001
Sutherland R. S., Dopita M. A., 1993, ApJS, 88, 253
Tegmark M. et al., 2004, ApJ, 606, 702
Tempel E., Libeskind N. I., 2013, ApJ, 775, L42
Tempel E., Stoica R. S., Saar E., 2013, MNRAS, 428, 1827
Teyssier R., 2002, A&A, 385, 337
Thatte N. et al., 2010, in Proc. SPIE Conf. Ser. Vol. 77352I, Ground-based and Airborne Instrumentation for Astronomy III. SPIE, Bellingham, p. 77352I
Tojeiro R. et al., 2017, MNRAS, 470, 3720
Trowland H. E., Lewis G. F., Bland-Hawthorn J., 2013, ApJ, 762, 72
Trujillo I., Carretero C., Patiri S. G., 2006, ApJ, 640, L111
Tully R. B., Fisher J. R., 1978, in Longair M. S., Einasto J., eds, IAU Symp. Vol. 79, Large Scale Structures in the Universe. Springer, Dordrecht, p. 31
Tweed D., Devriendt J., Blaizot J., Colombi S., Slyz A., 2009, A&A, 506, 647
Welker C., Devriendt J., Dubois Y., Pichon C., Peirani S., 2014, MNRAS, 445, L46
Welker C., Dubois Y., Pichon C., Devriendt J., Chisari E. N., 2015, preprint (arXiv:1512.00400)
Welker C., Dubois Y., Devriendt J., Pichon C., Kaviraj S., Peirani S., 2017, MNRAS, 465, 1241
White S. D. M., 1984, ApJ, 286, 38
White S. D. M., Rees M. J., 1978, MNRAS, 183, 341
Wright A. H. et al., 2016, MNRAS, 460, 765
Zel'dovich Y. B., 1970, A&A, 5, 84

APPENDIX A: MATCHING TECHNIQUE

A1 Mass matching

This Appendix provides details on the mass matching procedure. First the mass distributions of the two populations are cut so that they cover the same stellar mass range, i.e. they have the same minimum and maximum value of stellar mass. Then, in each stellar mass bin, the population with lower number of galaxies is taken as the reference sample and $N_{\rm match}$ samples of galaxies are extracted in the other population, such that their mass distribution is the same as the one of the reference sample. In practice, for each galaxy in the reference sample, the corresponding galaxy of the larger sample is sought among galaxies whose mass difference with respect to the reference mass is smaller than $\Delta M_\star$ in logarithmic space. If there is no galaxy in larger sample satisfying this condition, the galaxy of the reference sample is removed from the analysis. In each of $N_{\rm match}$ samples, every galaxy of the larger sample is considered only once, however repetitions are allowed across all samples. By construction, after applying this procedure, one ends up with $N_{\rm match}$ samples consisting of the same number of star-forming and passive galaxies and having very similar stellar mass distributions.

If not stated differently, 20 mass-matched samples are typically constructed using 10 equipopulated stellar mass bins for each and choosing a value of 0.1 for $\Delta M_\star$ parameter. Varying the values

of $N_{\rm match}$, $\Delta M_\star$ and the number of stellar mass bins within the reasonable range does not alter our conclusions.

A2 Density matching

This Appendix provides details on the density matching procedure. First, let us describe how the mass-density matched samples are constructed. The galaxy sample is first divided into three logarithmic stellar mass bins for which the density matched samples are to be constructed. In each of the 10 equipopulated logarithmic overdensity $(1+\delta)$ bins, the reference sample is identified as that of the previously constructed stellar-mass subsamples with the lowest number of galaxies. Next, for each galaxy in the reference sample, a galaxy is randomly chosen from each of two stellar mass bins having the overdensity closest to the galaxy in the reference sample. In practice, the nominal absolute difference in the $\log(M_\star/{\rm M}_\odot)$ values used to match galaxies is 0.1. If no suitable galaxy is found in at least one of the two stellar mass bins, the galaxy of the reference sample is removed from the analysis. This procedure is repeated 10 times, ending up with 10 samples of galaxies having the same overdensity distributions in three different stellar mass bins.

Similarly, to construct type-density matched samples, the entire galaxy sample is first divided into the subsamples of star-forming and passive galaxies. Then, in each of the 10 equipopulated logarithmic overdensity $(1+\delta)$ bins, the reference sample (sample of passive or star-forming galaxies) is identified as the one having the lowest number of galaxies. We continue by randomly choosing a galaxy from the larger sample with an overdensity and stellar mass close to that of the galaxy from the reference sample. In practice, we pair galaxies for which the distance in the two-parameter logarithmic space, defined by the stellar mass and the overdensity, is minimal and smaller than 0.1. The procedure is again repeated 10 times in order to construct 10 samples of star-forming and passive galaxies having their mass and density distributions close to each other.

APPENDIX B: THE IMPACT OF COSMIC BOUNDARIES

It was stated in Sections 4.2.1 and 4.3 that the measured gradients towards filaments (Figs 6 and 7) and walls (Figs 9 and 10) are not simply due to gradients towards nodes in the former and due to gradients towards nodes and filaments in the latter case. This Appendix presents the performed tests that allowed us to reach such a conclusion.

B1 Gradients towards filaments

Let us start by considering the gradients towards filaments. In order to probe these gradients without being substantially contaminated by the contribution from nodes, galaxies that are closer to nodes than 3.5 Mpc are removed from the analysis. The choice of this distance $d_{\rm min}^{\rm node}$ is motivated by the compromise between eliminating the most of the gradient coming from nodes while keeping enough objects to have a statistically significant sample. Note that the distance of 3.5 Mpc is greater than the typical size of groups, which is ~ 1.5 Mpc in the redshift range considered in this work, measured as a median (or mean) projected group radius. The value of median (and mean) is insensitive to the definition of the group radius (see Robotham et al. 2011, for various definitions considered). In Fig. B1, the solid lines show the mass gradients towards filaments for the entire sample (left-hand panel) on the one hand and after excluding galaxies with distances to the node $D_{\rm node} \leq 3.5$ Mpc (right-hand panel).

The contribution of nodes to mass gradients towards filaments is measured by randomizing distances to the filament, $D_{\rm skel}$, in bins of distances to the node, $D_{\rm node}$. By construction, gradients towards nodes are preserved. 20 samples are constructed in each of which this reshuffling method is applied in 20 equipopulated logarithmic bins. As shown by the dashed lines in Fig. B1 and values of medians listed in Table F1, the reshuffling cancels the gradients towards filaments for $d_{\rm min}^{\rm node} = 3.5$ Mpc.

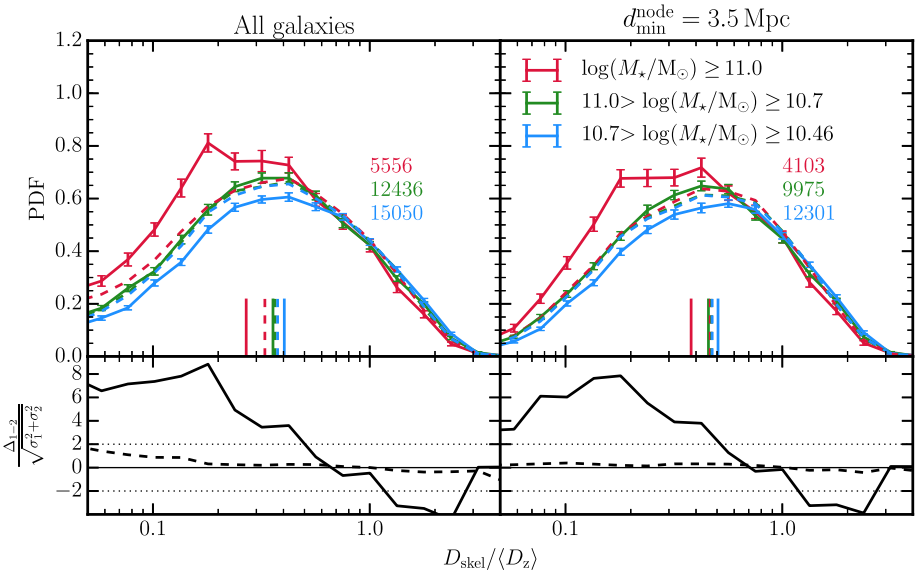

Figure B1. *Top row:* Differential distributions of the normalized distances to the nearest filament, $D_{\rm skel}$. The solid lines show mass gradients for all galaxies (left-hand panel) and after removing galaxies with distances to the node smaller than 3.5 Mpc (right-hand panel). The dashed lines illustrate mass gradients after the reshuffling of $D_{\rm skel}$ of galaxies in bins of distances to the node $D_{\rm node}$. The vertical lines indicate the medians of the distributions and their values, together with associated errors, are listed in Table F1. The reshuffling method cancels mass gradients towards filaments once galaxies at distances closer than 3.5 Mpc from nodes are removed. *Bottom row:* Residuals in units of σ between the two most extreme mass bins ($\log(M_\star/{\rm M}_\odot) \geq 11.0$ and $10.7 > \log(M_\star/{\rm M}_\odot) \geq 10.46$) before (solid lines) and after (dashed lines) the reshuffling.

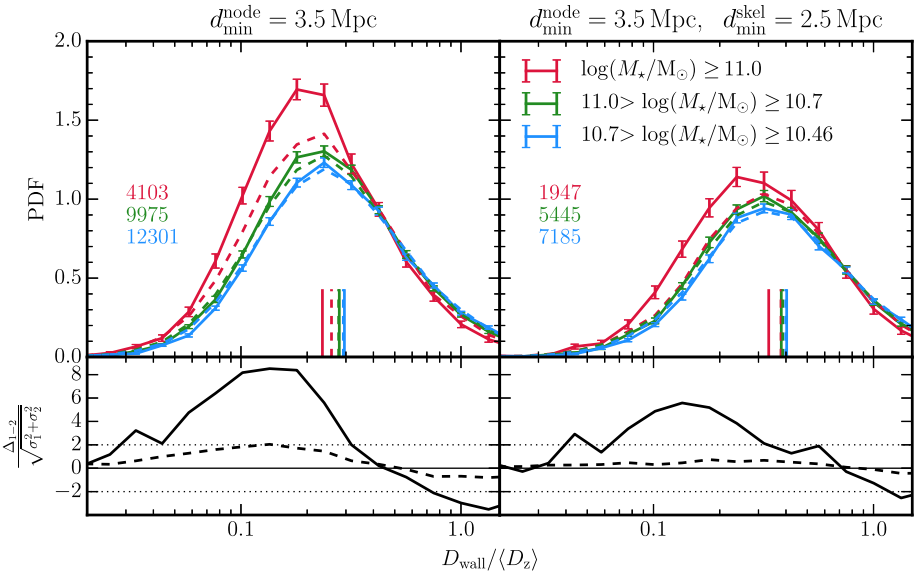

Figure B2. *Top row:* Differential distributions of the normalized distances to the nearest wall, $D_{\rm wall}$. The solid lines show mass gradients after removing galaxies with distances to the node smaller than 3.5 Mpc (left) and after applying an additional criterion on the distance to the filament, such that galaxies with distances to the filament smaller than 2.5 Mpc (right) are removed. The dashed lines illustrate mass gradient after reshuffling of $D_{\rm skel}$ of galaxies in bins of distances to the node $D_{\rm node}$. As shown on the right-hand panel, these are almost completely cancelled after removing sufficiently large regions around nodes and filaments. The vertical lines indicate the medians of the distributions and their values, together with associated errors, are listed in Table F2. *Bottom row:* Residuals are in units of σ as in Fig. B1.

In addition, following Laigle et al. (2017), it can be shown that in the regions sufficiently far away from nodes, gradients towards nodes and those towards filaments are independent. It was checked that the mass gradients towards nodes, present for the entire galaxy sample, are substantially reduced once galaxies for which distances to the node $D_{\rm node} \leq 3.5$ Mpc are excluded. This time, the distances to the node, $D_{\rm node}$, were randomized in bins of distances to the filament, $D_{\rm skel}$, i.e. by construction, gradients towards filaments were preserved. Again, 20 samples were constructed using 20 equipopulated logarithmic bins. After reshuffling, weak gradients at the level of at most 1σ are still present, but note that additional increase in $d_{\rm min}^{\rm node}$ does not reduce them further.

This analysis allows us to conclude that by removing from our sample galaxies that are closer to nodes than 3.5 Mpc, the impact of nodes to the measured gradients towards filaments is minimized, and even if weak gradients towards nodes still exist, these are independent of gradients towards filaments, i.e. gradients towards filaments and gradients towards nodes can be disentangled.

Let us finish this section with two remarks. First, note that distances to the node considered here are 3D euclidian distances. Curvilinear distances along the filaments could have been used instead (as illustrated in Fig. 4). This alternative choice of the distance does not alter our conclusions. Secondly, instead of using distances to the node $D_{\rm node}$, one could have considered distances normalized by the redshift-dependent mean inter-galaxy separation, $D_{\rm node}/\langle D_z \rangle$. These two approaches give consistent results not only qualitatively, but also quantitatively.

B2 Gradients towards walls

As with filaments, when measuring the gradients towards walls, one should investigate whether the gradient is not dominated by other component of the environments. As filaments are regions where walls intersect, these represent on top of nodes an additional source of contamination for the measured gradients towards walls. Fig. B2 shows the mass gradients towards walls for the galaxy sample outside the zone of influence of nodes parametrized by $d_{\rm min}^{\rm node} = 3.5$ Mpc (left-hand panel) and after applying an additional criterion by excluding galaxies with distances to the closest filament $D_{\rm skel} \leq d_{\rm min}^{\rm skel}$ with $d_{\rm min}^{\rm skel} = 2.5$ Mpc (right-hand panel). The contribution of filaments to the mass gradients towards walls is measured by randomizing distances to the wall, $D_{\rm wall}$, in bins of distances to the filament, $D_{\rm skel}$. By construction, the gradients towards filaments are preserved. Here 20 samples are constructed in each of which the reshuffling method is applied in 20 equipopulated logarithmic bins. As shown by the dashed lines in Fig. B2 and values of medians listed in Table F2, the reshuffling cancels the gradients towards walls for $d_{\rm min}^{\rm skel} = 2.5$ Mpc.

Following the method used in Appendix B1, it was verified (but not shown here) that the mass gradients towards filaments after randomization of the distances $D_{\rm skel}$ in bins of distances to the nearest wall $D_{\rm wall}$ are substantially reduced. Only a very weak mass gradient (at a 1σ level at most) is detected after randomization even for $d_{\rm min}^{\rm skel} = 2.5$ Mpc. Similarly to what was found in Section B1, increasing this parameter does not induce any substantial reduction of the gradient. Thus this distance was chosen as the limit for the exclusion region around filaments.

APPENDIX C: SMALL-SCALE DENSITY-COSMIC WEB RELATION

In this Appendix, the impact of the small-scale density estimator on the mass and type/colour gradients is presented. The density used here is DTFE, i.e. the density computed at the smallest possible scale.[10] As in Section 6, the two methods, the reshuffling and density-matching, are applied.

[10] There is no specific scale associated with the DTFE: it is a local adaptive method which determines the density at each point while preserving its multiscale character.

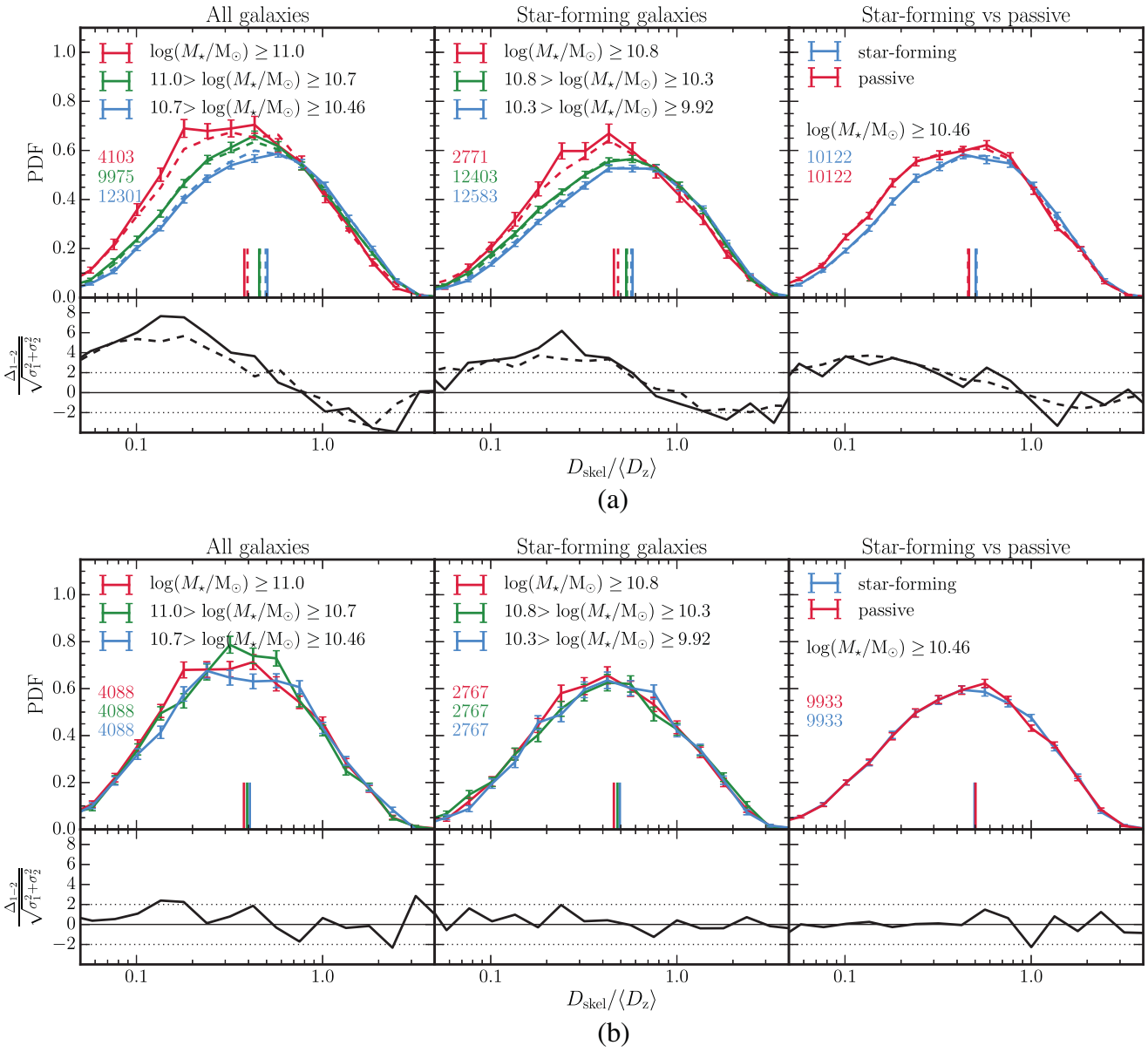

Figure C1. *Top rows:* As in Fig. 12, but using the DTFE density for both methods, reshuffling (Figure a) and density matching (Figure b). The numerical values of medians, shown as vertical lines, are listed in Table F3. When the small-scale density, DTFE in this case, is used in the reshuffling method, the randomized (dashed lines) and original signal (solid lines) are nearly identical. Similarly, all gradients are almost completely erased, as expected. *Bottom rows:* Residuals are in unit of σ as in Fig. 12. (a) Reshuffling. (b) Density matching.

Fig. C1 shows the differential distributions of the distances to the nearest filament, $D_{\rm skel}$ (normalized by $\langle D_z \rangle$, for the same selections as in Fig. 12. The contribution of the nodes to the measured signal is minimized, by removing from the analysis galaxies located closer to a node than 3.5 Mpc. Star-forming and passive galaxies have been matched in mass, as described in Appendix A1. The vertical lines indicate the medians of the distributions, whose values, together with the error bars, are listed in Table F3.

In Figure (a), the mass and type gradients are shown before (solid lines, as in 12) and after (dashed lines) applying the reshuffling of galaxies in the bins of overdensity $(1+\delta)$, where the number density corresponds to the DTFE density. The result conforms to the expectations. The reshuffling does not remove the observed mass and type/colour gradients, i.e. the distributions before and after the reshuffling are almost identical, suggesting that at the small scale, traced by DTFE, the density and cosmic web are closely correlated through the small-scale processes.

Figure (b) illustrates the PDFs for samples that have been matched in overdensity $(1 + \delta)$, as described in Appendix A2, where the density considered is DTFE. The density-matching technique yields qualitatively similar result than the above used reshuffling in that almost no mass and type gradients are detected when galaxies matched in the DTFE density.

Qualitatively same results are obtained for both methods when applied to the measurements of gradients with respect to the walls (not shown).

APPENDIX D: THE HORIZON-AGN SIMULATION

This Appendix is dedicated to presenting the large-scale cosmological hydrodynamical simulation HORIZON-AGN (Dubois et al. 2014). First, some of the main features of the simulation are briefly summarized. The reshuffling method is then implemented on the simulation, as defined in Section 6, and shown to yield qualitatively similar results to those obtained in GAMA for both large- and small-scale density tracers.

D1 Simulation summary

The detailed description of the HORIZON-AGN simulation[11] can be found in Dubois et al. (2014), here only its brief summary is given. The cosmological parameters used in the simulation correspond to the ΛCDM cosmology with total matter density $\Omega_{\rm m} = 0.272$, dark energy density $\Omega_\Lambda = 0.728$, amplitude of the matter power spectrum $\sigma_8 = 0.81$, baryon density $\Omega_{\rm b} = 0.045$, Hubble constant $H_0 = 70.4\,{\rm km\,s^{-1}\,Mpc^{-1}}$ and $n_s = 0.967$ compatible with the WMAP-7 data (Komatsu et al. 2011).

The simulation was run with the Adaptive Mesh Refinement code RAMSES (Teyssier 2002) in a box of length $L_{\rm box} = 100\,h^{-1}\,{\rm Mpc}$ containing 1024^3 dark matter (DM) particles, with a DM mass resolution of $M_{\rm DM,res} = 8 \times 10^7\,{\rm M}_\odot$, and initial gas resolution of $M_{\rm gas,res} = 1 \times 10^7\,{\rm M}_\odot$.

The collisionless DM and stellar components are evolved using a particle-mesh solver. The dynamics of the gaseous component are computed by solving Euler equations on the adaptive grid using a second-order unsplit Godunov scheme.

The refinement is done in a quasi-Lagrangian manner starting from the initial coarse grid down to $\Delta x = 1$ proper kpc (seven levels of refinement) as follows: each AMR cell is refined if the number of DM particles in a cell is more than 8, or if the total baryonic mass in a cell is eight times the initial DM mass resolution. This results in a typical number of 7×10^9 gas resolution elements (leaf cells) in the HORIZON-AGN simulation at $z = 0$.

Heating of the gas from a uniform UV background takes place after redshift $z_{\rm reion} = 10$ following Haardt & Madau (1996). Gas is allowed to cool down to 10^4 K through H and He collisions with a contribution from metals using a Sutherland & Dopita (1993) model.

The conversion of gas into stars occurs in regions with gas density exceeding $\rho_0 = 0.1\,{\rm H\,cm^{-3}}$ following the Schmidt (1959) relation of the form $\dot{\rho}_* = \epsilon_* \rho_{\rm g}/t_{\rm ff}$, where $\dot{\rho}_*$ is the SFR mass density, $\rho_{\rm g}$ the gas mass density, $\epsilon_* = 0.02$ the constant star formation efficiency, and $t_{\rm ff}$ the local free-fall time of the gas.

Feedback from stellar winds, supernovae type Ia and type II are included into the simulation with mass, energy and metal release. HORIZON-AGN simulation takes also into account the formation of black holes (BHs) that can grow by gas accretion at a Bondi–Hoyle–Lyttleton rate capped at the Eddington accretion rate when they form a tight enough binary. The AGN feedback is a combination of two different modes (the so-called quasar and radio mode) in which BHs release energy in the form of heating or jet when the accretion rate is, respectively, above and below 1 per cent of Eddington, with efficiencies tuned to match the BH-galaxy scaling relations at $z = 0$ (see Dubois et al. 2012a, for details).

Galaxies are identified using the updated method (Tweed et al. 2009) of the AdaptaHOP halo finder (Aubert et al. 2004) directly operating on the distribution of stellar particles. Only galactic structures with a minimum of $N_{\rm min} = 100$ stellar particles are considered, which typically selects objects with masses larger than $2 \times 10^8\,{\rm M}_\odot$.

D2 Density reshuffling

Let us finally present the impact of the reshuffling method, as defined in Section 6, and the choice of the density tracer in the HORIZON-AGN simulation.

Fig. D1 illustrates that the result of reshuffling depends on the scale at which the density is computed. As expected, when using the small-scale density tracer, such as e.g. the DTFE density (Figure a), both mass and sSFR gradients are almost unchanged, while on sufficiently large scales, the gradients tend to cancel out (Figure b). The numerical value of the scale at which this happens is ∼5 Mpc. This is again in a qualitative agreement with the scale required in the GAMA survey, corresponding to the ∼1.5× mean inter-galaxy separation.

[11] http://www.horizon-simulation.org

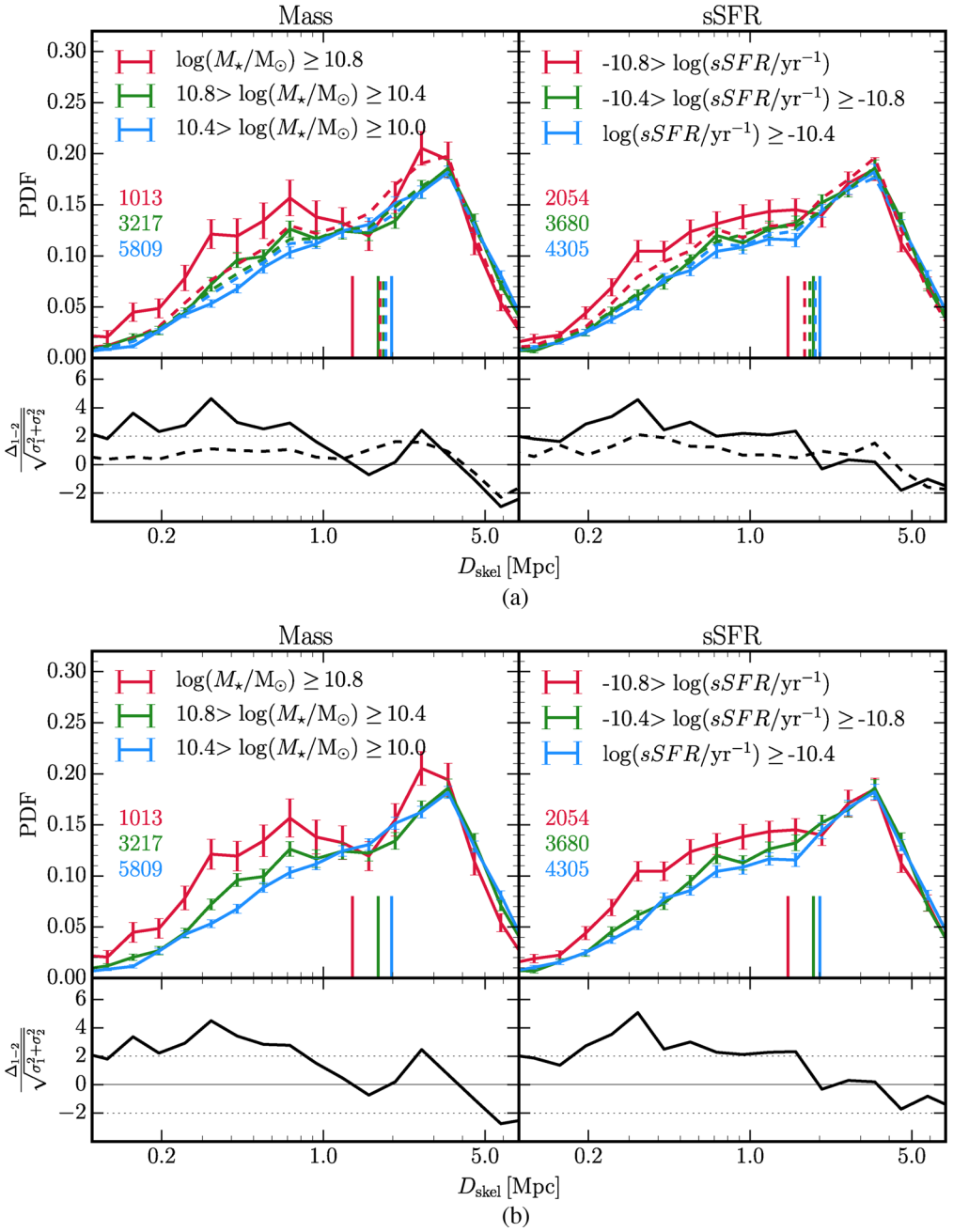

Figure D1. *Top rows:* As in Fig. 11 for the distances to the nearest filament, $D_{\rm skel}$. The contribution of the nodes is minimized by removing galaxies located within 3.5 Mpc around them from the analysis. The dashed lines correspond to the distributions after the application of the reshuffling method using two different density tracers, a large (Figure a) and small-scale (Figure b) estimators. The numerical values of medians, shown as vertical lines, are listed in Table F4. In qualitative agreement with the results obtained with the observed data, in order to cancel the gradients, density at sufficiently large scale has to be considered. This corresponds to 5 Mpc in the HORIZON-AGN simulation, representing $\sim 1.5\times$ mean inter-galaxy separation, again in agreement with the value found in observations. *Bottom rows:* As in Fig. 11 before (solid lines) and after (dashed lines) the reshuffling. (a) Reshuffling using the density computed in the Gaussian kernel at the scale of 5 Mpc. (b) Reshuffling using the DTFE density.

APPENDIX E: GRADIENT MISALIGNMENTS

In the context of conditional excursion set theory subject to a saddle $\mathcal{S}$ at some finite distance (r, θ, ϕ) from a forming halo, let us consider the Hessian of the potential, $q_{ij} \equiv \partial^2\psi/\partial r_i \partial r_j$, smoothed on the saddle scale $R_{\mathcal{S}}$ and normalized so that $\langle {\rm tr}^2(\boldsymbol{q})\rangle = 1$. The anisotropic shear is given by the traceless part $\bar{q}_{ij} \equiv q_{ij} - \delta_{ij}{\rm tr}\,\boldsymbol{q}/3$, which deforms the region by slowing down or accelerating the collapse along each axis. At finite separation, this traceless shear modifies in an anisotropic way the statistics of the smooth mean density (and of its derivative with respect to scale). The variations are modulated by $\mathcal{Q} = \sum_{i,j} \hat{r}_i \bar{q}_{ij} \hat{r}_j$, with $\hat{r}_i = r_i/r$, i.e. by the relative orientation of the separation vector, $\boldsymbol{r}$ in the frame set by the tidal tensor of the saddle. This extra degree of freedom, $\mathcal{Q}(\theta, \phi)$, provides a supplementary vector space, beyond the radial direction, over which to project the gradients, with statistical weight depending on each

specific observable (mass, accretion rate, etc.). These quantities have thus potentially different iso-surfaces from each other and from the local mean density, a genuine signature of the impact of the traceless part of the tidal tensor. Indeed, for each observable, the conditioning on $\mathcal{S}$ introduces a further dependence on the geometry of the environment (the height of the saddle and its anisotropic shear $\bar{q}_{ij}$) and on the position $\mathbf{r}$ of the halo with respect to the saddle point. This dependence arises because the saddle point condition modifies the mean and variance of the stochastic process $(\delta, \partial_R \delta)$ – the height and slope of the excursion set trajectories – in a position-dependent way, making it more or less likely to form haloes of given mass and assembly history within the environment set by $\mathcal{S}$. The expectation of the process becomes anisotropic through $\mathcal{Q}$, and both mean and variance acquire distinct radial dependence through the relevant correlation functions $\xi_{\alpha\beta}$ defined below in equation (E8).

For instance, considering the typical mass, $M_\star$ and accretion rate, $\dot{M}_\star$, at scale R, straightforward trigonometry shows that cross-product of their gradients reads

$$\left(\frac{\partial \dot{M}_\star}{\partial r}\frac{\partial M_\star}{\partial \mathcal{Q}} - \frac{\partial \dot{M}_\star}{\partial \mathcal{Q}}\frac{\partial M_\star}{\partial r}\right)\tilde{\nabla}\mathcal{Q}\,, \tag{E1}$$

where $\tilde{\nabla} = (\partial/\partial\theta, (1/\sin\theta)\partial/\partial\phi)$. The companion paper (Musso et al. 2017) shows that the Taylor expansion in the anisotropy for the angular variation, $\mathcal{Q}$, of $M_\star$ and $\dot{M}_\star$ at fixed distance r from the saddle scale like

$$\Delta M_\star \propto \xi_{20}(r)\mathcal{Q}(\theta,\phi)\,, \tag{E2}$$

and

$$\Delta \dot{M}_\star \propto \left[\xi'_{20}(r) - \frac{\sigma - \boldsymbol{\xi}'\cdot\boldsymbol{\xi}}{\sigma^2 - \boldsymbol{\xi}\cdot\boldsymbol{\xi}}\xi_{20}(r)\right]\mathcal{Q}(\theta,\phi)\,, \tag{E3}$$

in terms of the variance

$$\sigma^2(R) = \int \mathrm{d}k \frac{k^2 P(k)}{2\pi^2} W^2(kR)\,, \tag{E4}$$

and the radius-dependent vectors

$$\boldsymbol{\xi}(r) \equiv \{\xi_{00}(r), \sqrt{3}\xi_{11}(r)r/R_\star, \sqrt{5}\xi_{20}(r)\}\,, \tag{E5}$$

$$\boldsymbol{\xi}'(r) \equiv \{\xi'_{00}(r), \sqrt{3}\xi'_{11}(r)r/R_\star, \sqrt{5}\xi'_{20}(r)\}\,, \tag{E6}$$

where

$$R_\star^2 \equiv \int \mathrm{d}k \frac{P(k)}{2\pi^2}\frac{W^2(kR_\mathcal{S})}{\sigma_\mathcal{S}^2}\,, \tag{E7}$$

with $P(k)$ the underlying power spectrum, $W(k)$ the top hat filter in Fourier space, $\sigma_\mathcal{S} = \sigma(R_\mathcal{S})$, while the finite separation correlation functions, $\xi_{\alpha\beta}(r, R, R_\mathcal{S})$ and $\xi'_{\alpha\beta}(r, R, R_\mathcal{S})$ are defined as

$$\xi_{\alpha\beta} \equiv \int \mathrm{d}k \frac{k^2 P(k)}{2\pi^2} W(kR)\frac{W(kR_\mathcal{S})}{\sigma_\mathcal{S}}\frac{j_\alpha(kr)}{(kr)^\beta}\,, \tag{E8}$$

$$\xi'_{\alpha\beta} \equiv \int \mathrm{d}k \frac{k^2 P(k)}{2\pi^2} W'(kR)\frac{W(kR_\mathcal{S})}{\sigma_\mathcal{S}}\frac{j_\alpha(kr)}{(kr)^\beta}\,, \tag{E9}$$

where $j_\alpha(x)$ are the spherical Bessel functions of the first kind and prime denote derivate with respect to σ. Note that equation (E3) clearly highlights the shifted variance, $\sigma^2 - \boldsymbol{\xi}\cdot\boldsymbol{\xi}$, which contributes to the difference between $\Delta M_\star$ and $\Delta \dot{M}_\star$. From equation (E3), since the square bracket is not proportional to ξ_{20} as in equation (E2), it follows that the cross-product in equation (E1) is non-zero, which in turn implies that the contours of mass and accretion rate differ.

APPENDIX F: MEDIANS OF DISTRIBUTIONS

This Appendix gathers tables of medians with corresponding error bars used in previous sections.

Table F1. Medians of $D_{\rm skel}/\langle D_{\rm z}\rangle$ for Fig. B1.

Selection[a]	Mass bin	Median[b] $D_{\rm skel}/\langle D_{\rm z}\rangle$	
		Before reshuffling[c]	After reshuffling
All galaxies	$\log(M_\star/{\rm M}_\odot) \geq 11$	0.27 ± 0.01	0.33 ± 0.02
	$11 > \log(M_\star/{\rm M}_\odot) \geq 10.7$	0.36 ± 0.01	0.37 ± 0.01
	$10.7 > \log(M_\star/{\rm M}_\odot) \geq 10.46$	0.40 ± 0.01	0.38 ± 0.01
$d_{\rm min}^{\rm node} = 3.5$ Mpc	$\log(M_\star/{\rm M}_\odot) \geq 11$	0.38 ± 0.01	0.46 ± 0.02
	$11 > \log(M_\star/{\rm M}_\odot) \geq 10.7$	0.46 ± 0.01	0.47 ± 0.01
	$10.7 > \log(M_\star/{\rm M}_\odot) \geq 10.46$	0.51 ± 0.01	0.47 ± 0.01

[a]Panels of Fig. B1.
[b]Medians of distributions as indicated in Fig. B1 by vertical lines; errors are computed as in Table 1.
[c]Randomization of $D_{\rm skel}$ in bins of $D_{\rm node}$.

Table F2. Medians of $D_{\rm wall}/\langle D_z\rangle$ for Fig. B2.

Selection[a]	Mass bin	Median[b] $D_{\rm wall}/\langle D_{\rm z}\rangle$	
		Before reshuffling[c]	After reshuffling
$d_{\rm min}^{\rm node} = 3.5$ Mpc	$\log(M_\star/{\rm M}_\odot) \geq 11$	0.234 ± 0.005	0.258 ± 0.011
	$11 > \log(M_\star/{\rm M}_\odot) \geq 10.7$	0.279 ± 0.003	0.278 ± 0.005
	$10.7 > \log(M_\star/{\rm M}_\odot) \geq 10.46$	0.295 ± 0.003	0.292 ± 0.004
$d_{\rm min}^{\rm node} = 3.5$ Mpc, $d_{\rm min}^{\rm skel} = 2.5$ Mpc	$\log(M_\star/{\rm M}_\odot) \geq 11$	0.334 ± 0.007	0.379 ± 0.028
	$11 > \log(M_\star/{\rm M}_\odot) \geq 10.7$	0.381 ± 0.004	0.386 ± 0.011
	$10.7 > \log(M_\star/{\rm M}_\odot) \geq 10.46$	0.403 ± 0.004	0.398 ± 0.008

[a]Panels of Fig. B2.
[b]Medians of distributions as indicated in Fig. B2 by vertical lines; errors are computed as in Table 1.
[c]Randomization of $D_{\rm wall}$ in bins of $D_{\rm skel}$.

Table F3. Medians for the PDFs displayed in Fig. C1: small-scale density

	Selection[a]	Bin	Median[b] $D_{\rm skel}/\langle D_{\rm z}\rangle$ Original[c]	reshuffling[d]	Matching[e]
Masses	All galaxies	$\log(M_\star/{\rm M}_\odot) \geq 11$	0.379 ± 0.009	0.397 ± 0.009	0.378 ± 0.01
		$11 > \log(M_\star/{\rm M}_\odot) \geq 10.7$	0.456 ± 0.007	0.459 ± 0.006	0.393 ± 0.009
		$10.7 > \log(M_\star/{\rm M}_\odot) \geq 10.46$	0.505 ± 0.006	0.495 ± 0.006	0.406 ± 0.008
		$\log(M_\star/{\rm M}_\odot) \geq 10.8$	0.459 ± 0.012	0.489 ± 0.013	0.458 ± 0.011
	SF galaxies	$10.8 > \log(M_\star/{\rm M}_\odot) \geq 10.3$	0.534 ± 0.007	0.541 ± 0.008	0.479 ± 0.01
		$10.3 > \log(M_\star/{\rm M}_\odot) \geq 9.92$	0.578 ± 0.007	0.567 ± 0.007	0.494 ± 0.006
Types	SF versus passive[f]	Star-forming	0.504 ± 0.008	0.508 ± 0.007	0.495 ± 0.006
		Passive	0.462 ± 0.007	0.458 ± 0.007	0.504 ± 0.006

[a]Panels of Fig. C1.
[b]Medians of distributions as indicated in Fig. C1 by vertical lines; errors are computed as in Table 1.
[c]As in Table 1 for $D_{\rm skel}/\langle D_{\rm z}\rangle$.
[d]Reshuffling is done in bins of DTFE density (see the main text for more details).
[e]Medians for the density-matched sample, where the density considered is DTFE.
[f]Only galaxies with stellar masses $\log(M_\star/{\rm M}_\odot) \geq 10.46$ are considered.

Table F4. Medians for the PDFs displayed in Fig. D1

Selection[a]	Bin	Median[b] $D_{\rm skel}$ [Mpc] Original[c]	after reshuffling[d] DTFE	G5Mpc
Mass	$\log(M_\star/{\rm M}_\odot) \geq 10.8$	1.34 ± 0.09	1.26 ± 0.08	1.72 ± 0.1
	$10.8 > \log(M_\star/{\rm M}_\odot) \geq 10.4$	1.73 ± 0.08	1.71 ± 0.06	1.82 ± 0.06
	$10.4 > \log(M_\star/{\rm M}_\odot) \geq 10$	1.97 ± 0.04	2.0 ± 0.05	1.86 ± 0.04
sSFR	$-10.8 > \log(sSFR/{\rm yr})$	1.46 ± 0.07	1.61 ± 0.07	1.74 ± 0.08
	$-10.4 > \log(sSFR/{\rm yr}) \geq -10.8$	1.88 ± 0.06	1.89 ± 0.06	1.81 ± 0.06
	$\log(sSFR/{\rm yr}) \geq -10.4$	2.0 ± 0.04	1.9 ± 0.05	1.91 ± 0.06

[a]Panels of Fig. D1.
[b]Medians of distributions as indicated in Fig. D1 by vertical lines; errors are computed as in Table 1.
[c]As in Table 2 for $D_{\rm skel}$ (corresponding to the solid lines in Fig. D1).
[d]Reshuffling is done in the bins of the DTFE density and the density computed at the scale of 5 Mpc (corresponding to the dashed lines in Figures a and b, respectively).

This paper has been typeset from a TEX/LATEX file prepared by the author.